Embedding fiber Bragg grating sensors through ultrasonic additive manufacturing

A Thesis

Presented in Partial Fulfillment of the Requirements for the Degree Master of Science in the Graduate School of The Ohio State University

By

John J Schomer, B.S.

Graduate Program in Mechanical Engineering

The Ohio State University

2017

Master's Examination Committee:

Dr. Marcelo J. Dapino, Advisor

Dr. Mo-How Shen

Abstract

Fiber Bragg Grating (FBG) sensorsare optical fibers that detect in-situ strain through deviation of a reflected wavelength of light to detect in-situ strain. These sensors are immune to electromagnetic interference, and the inclusion of multiple FBGs on the same fiber allows for a seamlessly integrated sensing network. FBGs are attractive for embedded sensing in aerospace applications due to their small noninvasive size and prospect of constant, real-time nondestructive evaluation. FBGs are typically used in composite laminate type applications due to difficulties in building them into metallic structures. Additive manufacturing, also referred to as 3D printing, can allow for the inclusion of sensors inside of structural entities by the building of material around the sensor to be embedded. In this study, FBG sensors are embedded into aluminum 6061 via ultrasonic additive manufacturing (UAM), a rapid prototyping process that uses high power ultrasonic vibrations to weld similar and dissimilar metal foils together. UAM was chosen due to the desire to embed FBG sensors at low temperatures, a requirement that excludes other additive processes such as selective laser sintering or fusion deposition modeling. This study demonstrated the feasibility of embedding FBGs in aluminum 6061 via UAM. Further, the sensors were characterized in terms of birefringence losses, post embedding strain shifts, consolidation quality, and strain sensing performance. Sensors embedded into an ASTM test piece were compared against an exterior surface mounted foil strain

gage at both room and elevated temperatures using cyclic tensile tests. The effects of metal embedment at temperatures above the melting point of the protective coating (160 degrees Celsius) of the FBG sensors were explored, and the hermetic sealing of the fiber within the metal matrix was used to eplain the coating survival. In-situ FBG sensors were also used to monitor the UAM process itself. Lastly, an example application was both modeled using finite element analysis to identify areas where FBG sensors could be placed, and then built with an embedded FBG sensor.

Acknowledgments

Vita

April 2nd, 1993 ....Born - Cleveland, Ohio

June 2011 ....Diploma, North Royalton High School

May 2015 ................................B.S. Aeronautical and Astronautical Engineering, The Ohio State Univeristy

June 2015 - August 2015 ....Intern, NASA Glenn Research Center

February 2012 - May 2015 ....Undergraduate Research Assistant, The Ohio State University

June 2015 - May 2016 ....Graduate Research Associate, The Ohio State University

Publications

Conference Proceedings

J.J. Schomer, A.J. Hehr, and M.J. Dapino. Characterization of embedded fiber optic strain sensors into metallic structures via ultrasonic additive manufacturing. In *SPIE Conference on Smart Structures and Materials, Nondestructive Evaluation and Health Monitoring*, Las Vegas, NV, March 2016.

Fields of Study

Major Field: Mechanical Engineering

  Studies in Smart Materials and Structures: Dr. Marcelo Dapino

Table of Contents

List of Tables

List of Figures

x

xi

Chapter 1: INTRODUCTION

1.1 Motivation

Structural health monitoring plays an important role in modern engineering by detecting damage prior to failure and allowing for efficient system maintenance. Being able to predict when preventative maintenance is required increases the lifetime of structures, and minimizes the need for excessive safety factors which drive up material and fuel costs in vehicles. While non-destructive evaluation of aircraft and other structures is typically performed using external devices, there are advantages to integrating in-situ sensors to obtain real time structural data. Embedded sensing allows for the measurement of mechanical signals within parts that cannot be easily monitored externally, such as curved beams, aircraft wings, and turbine blades. Embedded sensing can also meet requirements in structures subjected to harsh or extreme conditions, such as corrosive environments or applications which experience extreme temperatures. In these types of extreme applications, external sensors cannot survive. Another benefit of embedded sensing is that it allows for a more direct measurement of the state of the material matrix, and allows for the direct measurement of loads at critical areas within components. The incorporation of an embedded

sensing network also helps to create intelligent structures or systems, which refer to systems capable of responding to changes in their environments.

Sensors are typically embedded during the fabrication of a component or part for encapsulation. In the case of strain and load sensors, this is important as it encourages mechanical coupling between the matrix and the sensor at their connecting interface. In the case of Fiber Bragg Grating (FBG) sensors, this is often accomplished by placement in-between ply layers of laminated composites. [29, 30] This methodology presents difficulties in the fabrication of solid metallic entities with embedded sensing elements. Many such solid components are built through forging or machining, in which a liquid matrix never exists for the sensor to be placed into, or are liquid at temperatures high enough that the protective coatings used on the FBGs cannot survive, resulting in either core failure or non-uniform core loading. One method of addressing these issues is to build parts through additive manufacturing, or 3D printing.

Additive manufacturing refers to the fabrication of a part through the addition of material rather than the subtraction/reforming of a part. There are numerous ways to accomplish this, but it is typically done by placing material at its intended location, applying heat or some other form of energy, and bonding successive layers or powders together. The ability to form a part additively allows for sensing elements to be integrated into a structure by building the structure around the sensor. While the embedment of FBG sensors via 3D printing has been documented [1], there have been few attempts to provide a formal understanding of the mechanical coupling, reliability, and performance limits of FBGs after they have been embedded.

2

This study seeks to provide a method for effectively manufacturing parts made out of aluminum with embedded FBG sensors using commercially available protective coatings, to characterize the impacts of UAM on the performance of the sensors, to ensure meaningful data is obtained during sensing, and to investigate the operating limits of the sensors after encapsulation.

1.2   Ultrasonic Additive Manufacturing

The 3D printing method used for this study was Ultrasonic Additive Manufacturing (UAM). This process allows for the fabrication of metallic parts comprised of either similar or dissimilar metals through the Ultrasonic Welding (UW) of layers of metallic tape onto a baseplate. Welds are accomplished through the scrubbing of metals together at ultrasonic frequencies and high contact force as shown in Figure 1.1, in turn disrupting and expelling the oxide layers between metal surfaces and encouraging plastic deformation and the flow of grains between the tape and structure at the interface [9]. This allows for direct contact between nascent metallic surfaces. This direct contact encourages diffusion, and combined with the intermixing of grains and recrystallization allows for bonding of the materials without melting. UW welding creates solid state bonds, and operates at low local temperatures since melting is not required.
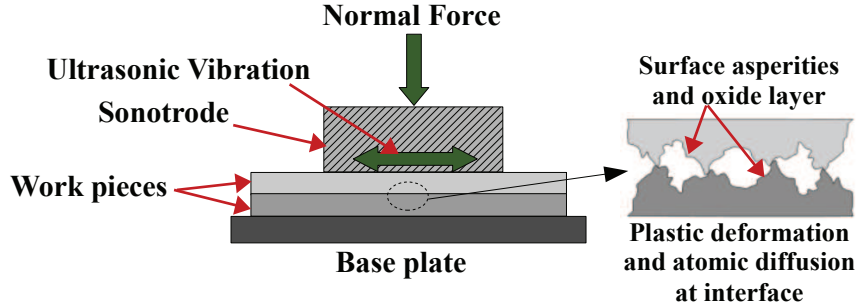
Figure 1.1: UAM bonding works by scrubbing the metallic surfaces of foil and build structure together to create a solid state bond.

In the case of UAM, scrubbing is accomplished by a welding horn, driven by piezoelectric transducers to vibrate at 20 kHz, which rolls over the tape and build surface, in contrast to typical spot welding used in UW applications. The ultrasonic vibrations are guided through the weld assembly such that a standing wave forms at the weld head surface, which directs the ultrasonic energy into the tape. The horn itself is machined to have substantial surface roughness, which allows for the horn to grip the tape and increase interfacial deformation. The weld parameters typically controlled during UAM and other ultrasonic bonding processes are vibration amplitude, welder normal force, process temperature, and weld speed. It has been shown in the literature that a stronger bonding occurs in the 'z' direction of builds (up/down during the build process) when the normal force is higher, the weld speed is lower, the vibration amplitude is higher, and the ambient temperature is higher. Very High Power (VHP) UAM is a variant of UAM which is performed on a machine capable of producing up to 9 kW of weld power, in contrast to earlier UAM machines

which were limited to 1 kW. VHP UAM allows for stronger, more aggressive weld parameters to achieve stronger bonding. The weld assembly is shown in Figure 1.2.
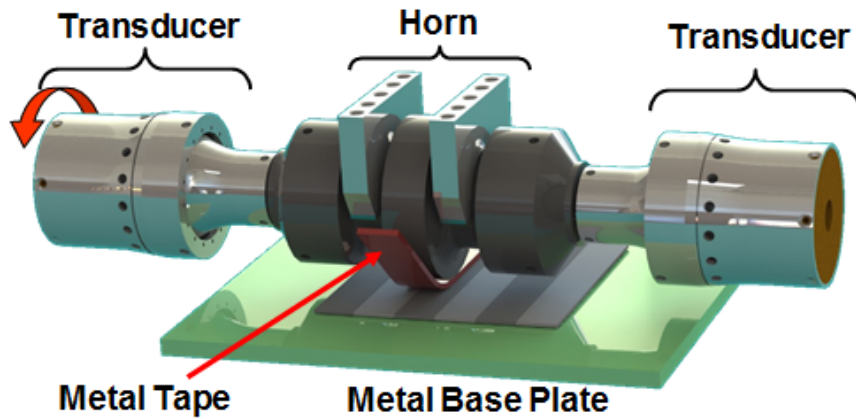
Figure 1.2: UAM Weld assembly. The horn is driven by piezoelectric transducers as it rolls over metal tapes to create a solid state bond

As the weld assembly is built into a CNC framework shown in figure 1.3, periodic machining operations can be included into UAM part design. This allows for the seamless inclusion of channels, sensing elements, circuitry, and other types of complex internal features in UAM structures that are not possible using conventional, non additive manufacturing methods. The low temperature of the process also helps with embedding features that are either sensitive too or damaged by elevated temperatures. These aspects of UAM together form a process with unprecedented capability to create smart structures, which are structures that can detect or respond to changes in their environment or state. Previous studies on the use of UAM to embed optical fiber have focused on successful embedding of non-graded fiber into an aluminum matrix,

5

reducing damage to the fiber, and thermomechanical response testing of FBGs. These studies were able to transmit light through embedded fibers, embed multiplexed FBGs into aluminum, and measure residual strain on the FBGs resulting from the UAM process. [5, 14]
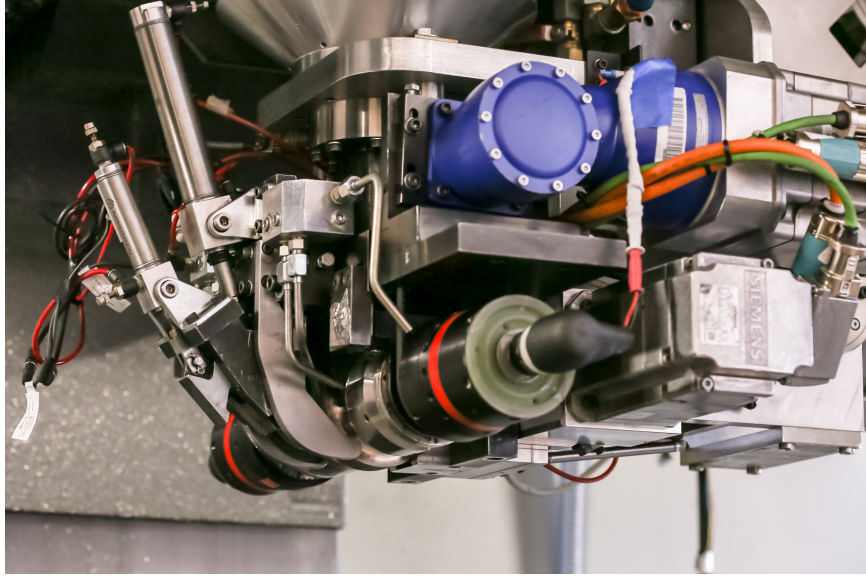
Figure 1.3: UAM Weld assembly in CNC machine

1.3   Fiber Bragg Grating Sensors

Fiber Bragg Grating (FBG) sensors are used for real-time in-situ measurement of strain and temperature. FBG sensors refer to a grating inscribed upon an optical fiber, consisting of a glass core, a glass cladding, and an external protective coating shown in Figure 1.4. Optical fibers are built such that the refraction planes within the silica glass core and cladding are perpendicular, which encourages nearly total internal reflection of light throughout the fiber. The FBG sensor consists of individual gratings

etched into the glass using a UV laser [13]. These gratings are placed a uniform distance from each other, such that resonance can be induced upon an incoming light signal of a specific wavelength. When a broadband spectrum of light (white light) is sent through the fiber, this specific wavelength resonates within the grating, and some of the signal is reflected back towards the source. Figure 1.5 shows that when the distance between gratings changes as a result of either mechanical or thermal strain, a different wavelength is reflected towards the source. The change in this wavelength is measured and compared to the initial, nominal strain wavelength of the FBG, and the strain of the sensor can be calculated from this wavelength change as it has a linear relationship. FBGs are used in embedded sensing applications such as composite pressure vessels, composite lap joints, and composite manufacturing processes, and show promise for being embedded into monolithic metal structures. [10] Since FBG sensing networks are based on measuring light, the sensors themselves are immune to electromagnetic noise/interference. FBG sensors have potential uses in high-temperature strain sensing applications due to the high melting point of silica glass (over 1000 degrees Celsius) [15]. The incorporation of multiple FBG sensors in the same fiber is referred to as multiplexing, and is either accomplished through giving FBGs different wavelengths or by using detector timeslots to seperate the data based on when it was recieved [16]. This can allow for a complex sensing network to be incorporated via the integration of a single fiber into a structure. So long as a sufficient length of fiber is embedded into the matrix material being measured and the load on along the sensor is uniform, consistent and real-time structural health monitoring can be achieved.

7
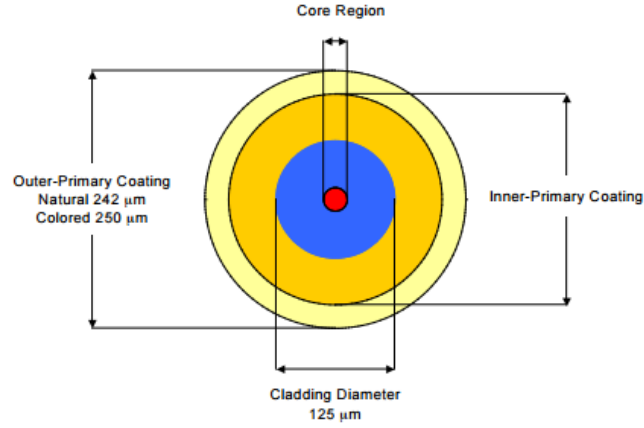
Figure 1.4: FBG cross-section: A UV cured dual-acrylate protective coating is placed on a silica glass cladding and core, and near total-internal-reflection within the core allows for light to be transmitted with low losses.
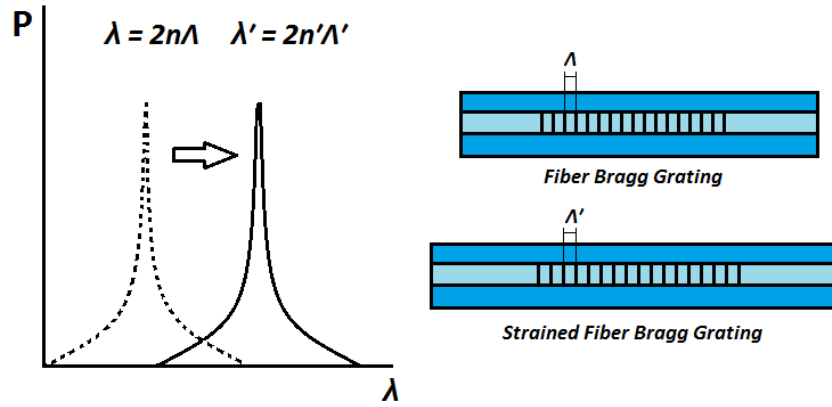
Figure 1.5: FBG sensing: as the FBG is strained, the grating spacing increases, and an associated change in reflected wavelength takes place.

The commercially used standard protective coating used for FBGs is UV cured dual-acrylate. While standard acrylate has a well documented melting temperature

8

of 160 degrees Celsius [17, 19, 4], the UV cure process alters the chemical makeup of the acrylate used in FBG applications [20, 22]. As such, when exposed to temperatures above 80 degrees Celsius, the coatings degrade or carbonize over time following the profiles shown in Figure 1.6. This carbonization process has been shown to be dependent on both the heating rate and gas content of the atmosphere that the FBG is placed in, and has been shown to be non-linear, multi-stage process [2]. For high temperature sensing applications (100-400 Celsius) polyamide coatings are typically used. Both acrylate and polyamide coated FBGs were embedded and characterized in terms of strain sensing at room and elevated temperatures. Since FBG sensors embedded into aluminum through UAM are sealed hermetically within the aluminum matrix, the impact of metal encapsulation on the carbonization process was also examined as part of this study. This was accomplished through tensile testing during which the sample was subjected to high ambient temperatures, and through oven testing in which K-type thermocouples were incorporated in the sample.
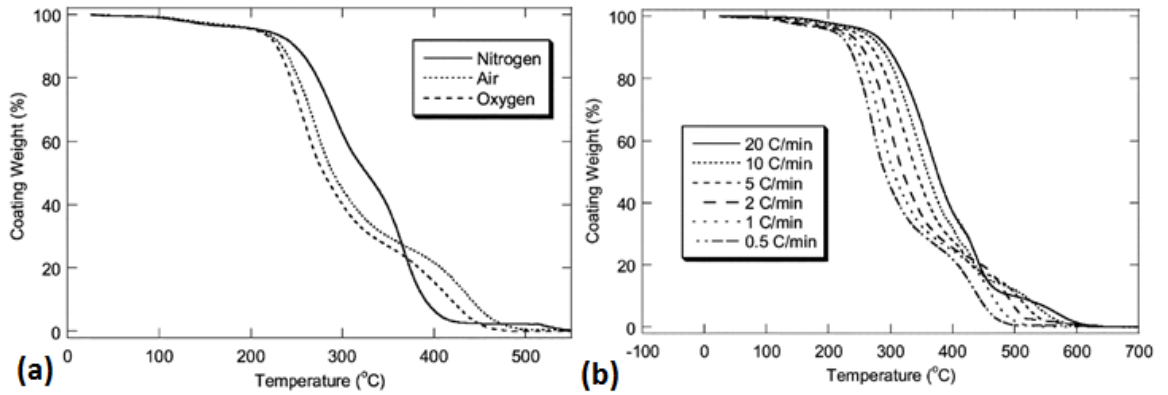
Figure 1.6: Experimental profiles of acrylate coating degradation [2]: (a) effect of gas environment; (b) effect of heating rate.

1.4 Shear Transfer Modeling

An FEA model was built that describes the shear transfer behavior from the aluminum matrix to the FBG. The purpose of this model was to shed light on the minimum sensor length, determined by the critical length in the shear lag equation. Shear lag is a phenomenon experienced by fibers in composite builds. It is the result of non-uniform loading occurring towards the ends of a composite build due to the mismatch in elastic modulus of materials, and the effect diminishes across the length of the embedded fiber. Figure 1.7 shows an example of how this phenomenon manifests.
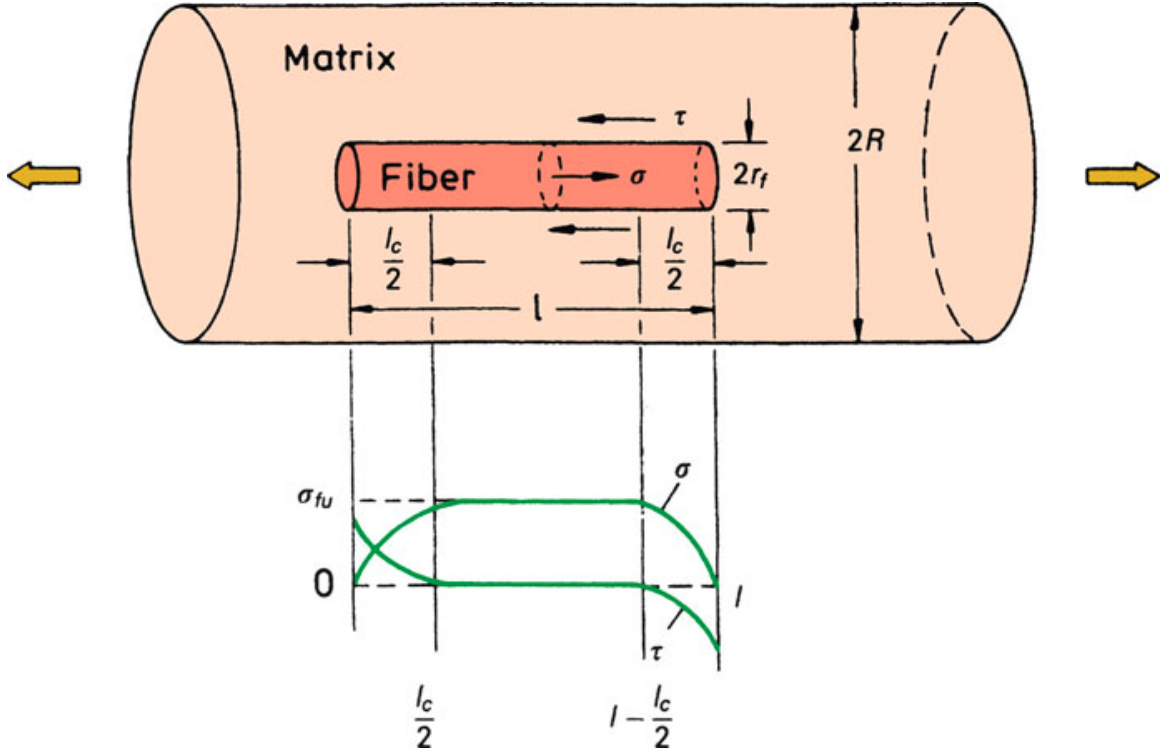
Figure 1.7: Shear lag within an embedded fiber. Note that the normal stress within the fiber is 0 at the ends, then increases to equal that of the surrounding matrix over half of the critical length [6].

It is important for FBG sensors to experience uniform loading in order to obtain useful data, as a non-uniform loading means that the distance between each of the gratings is no longer constant, and as such the minimum specimen length is determined by the critical length for shear lag. By modeling the matrix in COMSOL, a multiphysics platform, it was determined that the shear lag diminishes to negligible amounts within a few millimeters, meaning that so long as the FBG sensor is more than a few millimeters away from the ends of the specimen that a relatively uniform load profile can be expected. The COMSOL model assumed no boundary loads were placed on the fiber itself, which was consistent with a real loading that would be expected on an embedded fiber. Using this result, subsize tensile test specimens with a length of 3 in were designed, such that FBG sensors were located more than an inch away from the specimen ends. The model geometry and shear lag profile are shown in Figure 1.8.
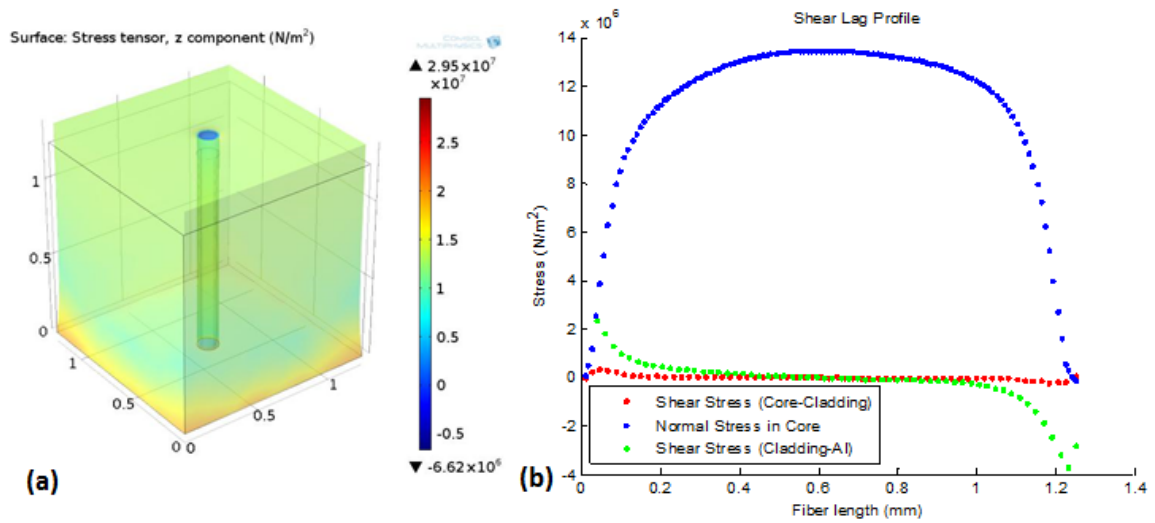
Figure 1.8: COMSOL shear lag model: (a) 3D composite geometry (b) stress within the fiber

1.5   Ultrasonic Metal Bonding Monitoring

Characterization of bonding quality during ultrasonic joining is not a novel field by any means, but it is one in which the literature is lacking. There are a number of good reasons for this; the process by which a bond actually forms is not fully understood, the interfacial nature of bonding requires sensors to be placed extremely close to the actual point of bonding, and the exact material properties of a 'good' bond are not well agreed upon. Despite this, several existing papers seek to provide some insight into the quality of bonding in real time using in-situ, non-destructive methods.

Two seperate studies utilized temperatures sensors for ultrasonic metal welding (UMW) [7, 11]. Since the sensors were embedded away from the weld surface, an exact thermal profile cannot be inferred from the data. There is potential usefulness in thermally sensitive applications, such as the embedment of shape memory alloy into aluminum. Since the exact load profile of the SMA is determined in part by the temperature, having a nearly exact profile of the temperature would be useful in addressing the response to future mechanical and thermal loads.
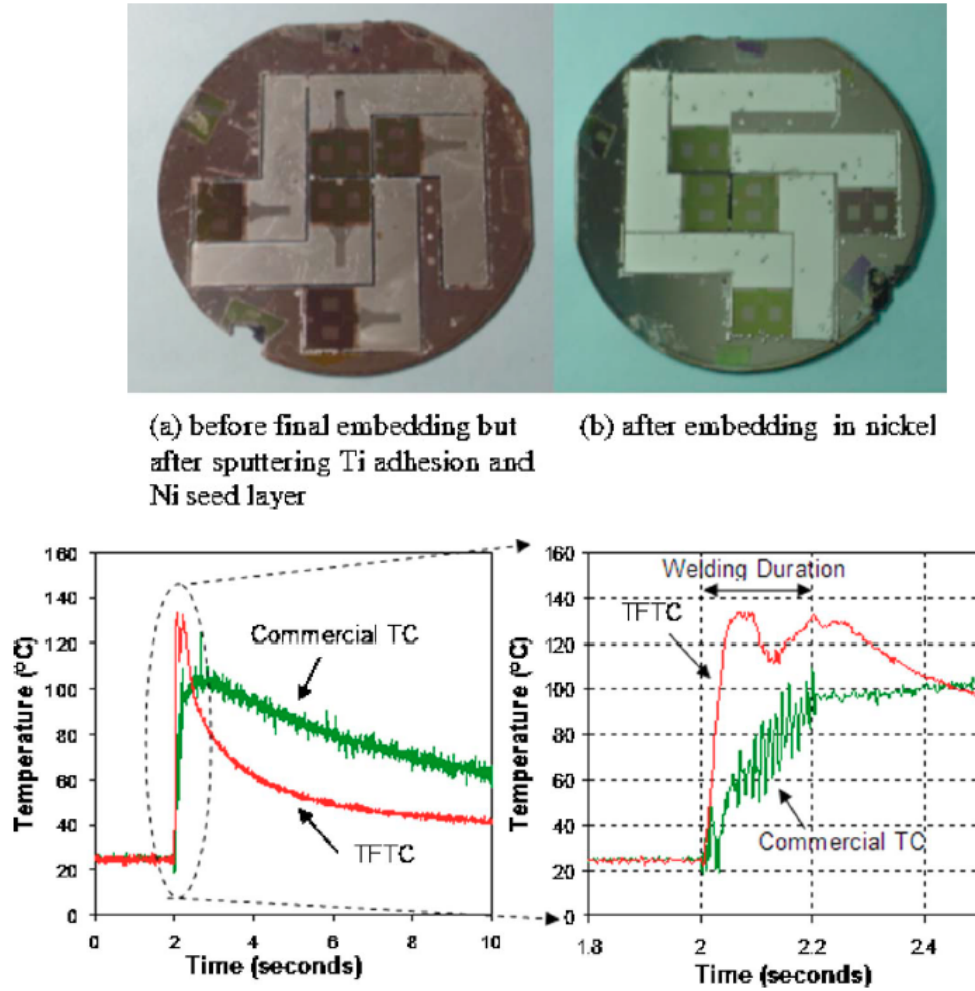
Figure 1.9: Thin film thermocouples embedded into nickel, and measurement comparison to commercial thermocouples during ultrasonic welding. [7]

In the case of some other studies of interest , power signal monitoring and high-speed imaging were used to infer weld quality [26, 25]. The primary measurement taken in these studies to verify weld quality was weld density, and while a lack of void character is necessary to show good bonding, it has been shown to not be sufficient. One such test setup is shown in Figure 1.10. Improving upon existing tests with

a more rigorous definition of quality bonding is an ongoing effort in the ultrasonic bonding community.
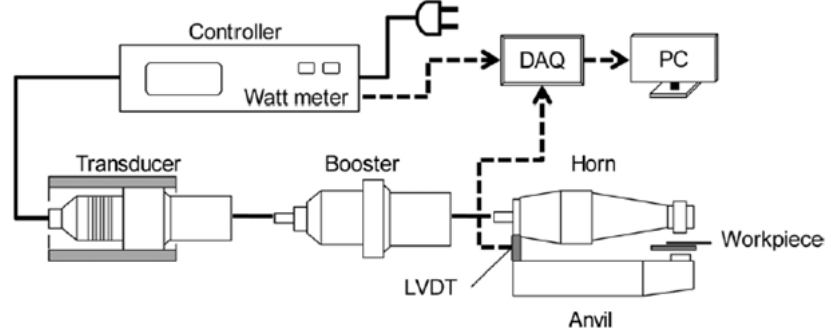
Figure 1.10: Monitoring of ultrasonic metal welding [26]

1.6 Embedded FBG Sensors

Embedding FBG sensors into metallic components is challenging due to the effects of thermal strain on the sensor during fabrication, coating degradation that occurs at elevated temperatures, and polarization losses induced by uneven cross-sectional loading of the fiber. Strain is transferred from the bulk material through the interface from simple mechanical coupling. As such, FBG sensors are most effective when directly built into plastic and metallic components for health monitoring. FBG sensors are brittle, which rules out conventional manufacturing methods that involve fusion of the matrix material. [28] Additive manufacturing, or 3D printing, is the method of adding material to fabricate a part rather than removing material, and offers unprecedented opportunities in the creation of smart structures,metal-matrix composite materials, and parts with complex internal geometries. Instead of inserting an FBG

14

sensor into a previously finished part or a composite, the part can be built around the existing sensor, resulting in a single piece plastic or metal structure with integrated sensing. Fused deposition modeling is a 3D printing method that outputs plastic parts, and is capable of incorporating FBGs. FBGs have been embedded though this process in order to measure residual stresses in parts after fabrication. [1] FBGs were also embedded into a polymeric sample made through selective laser sintering, an additive process in which powders are fused via a laser, and comparative strain measurements were taken from the FBG, an extensometer, and an externally mounted foil gage. [23] In the latter study, the sintering process temperatures were high enough to cause degradation of acrylate coated FBGs. Through the use of selective laser melting, FBGs were also embedded into a stainless-steel part in order to measure the residual strain from the process, but fabrication issues led to polarization errors and voids between the matrix material and the sensor. [8]
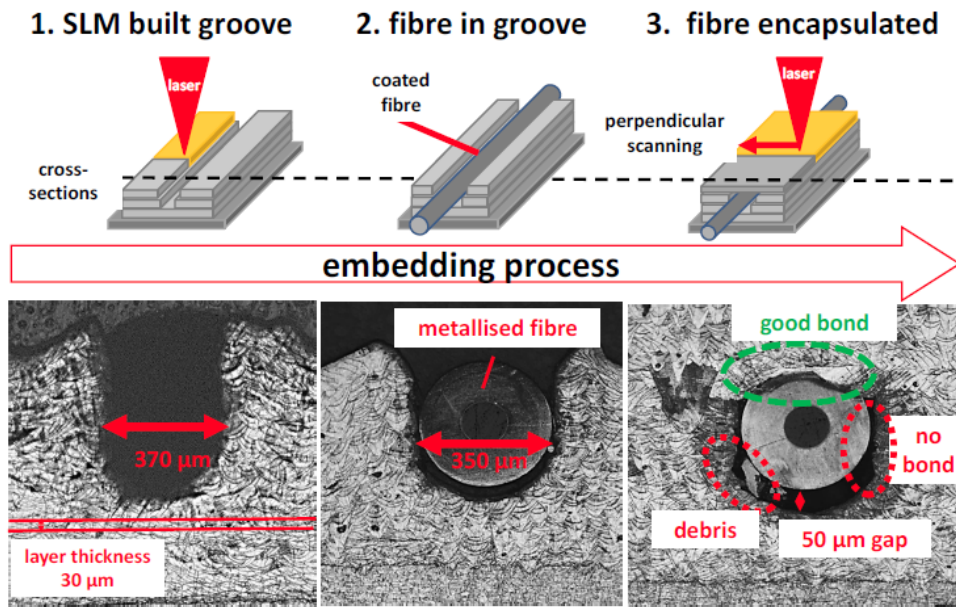
Figure 1.11: FBG embedded via selective laser melting [8]

Chapter 2: PROJECT PROCEDURES

2.1   Sample Fabrication

A pilot study was conducted on the survival of optical fiber embedded into an aluminum 6061 matrix through UAM. Several fabrication parameters impact both the specimen properties and the performance of embedded FBGs, including the amplitude, speed, and down force on the sonotrode [9, 18]. The UAM parameters used were 900 lb (4000 N) down force, room temperature, 200 in/m (508 cm/m) weld speed, and a weld amplitude of 0.0012 in (30-32 μm). To build the test specimens, two to three layers of aluminum 6061 tape were welded onto a 6061 baseplate in order to ensure that the fiber was entirely encapsulated in UAM welded aluminum, and was not in direct interfacial contact with bulk material. A channel of 0.010 in (0.254 mm) depth and equal width was then cut lengthwise across the surface sample using a ball-tipped end mill, and the fiber was positioned in the center of the test specimen. This channel was used to hold the fiber in place during the welding of the final layer of material. After temporarily securing the fiber, an encapsulating layer of aluminum foil was welded over the fiber. The sample shape, shown in Figure 2.1, was then traced using a 1/8th in (3.175 mm) diameter end mill, and the excess baseplate material was removed from the sample using the CNC features of the SonicLayer

4000. The fibers themselves were only held in place by friction, and no epoxy or electroplating of metal was required to encourage bonding. Industry standard SMF-28e optical fiber was used instead of FBGs to preserve material for the initial pilot study. Optical fiber with UV cured dual-acrylate coating and optical fiber that had been stripped of the acrylate through prolonged submersion in an acetone bath were both used. Stripped and electroplated fiber was not used, partially in an effort too minimize manufacturing complexity and also to see if FBGs utilizing commercially available coating could be embedded.
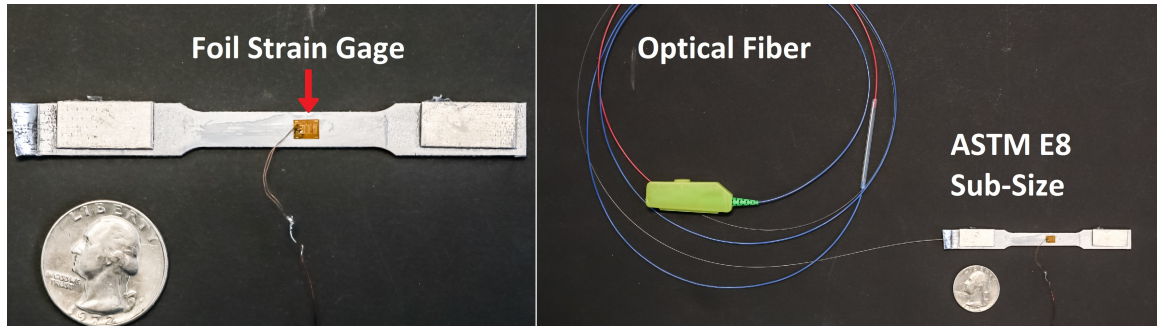
Figure 2.1: Example of a subsize tensile test specimen with embedded FBG sensor fabricated via UAM.

After core survival was shown, optical fibers containing FBG sensors were embedded into an aluminum 6061 matrix via UAM. The test specimens produced for this study were based on ASTM E8 standards [27], and were produced on a Fabrisonic SonicLayer 4000, shown in Figure 2.2. The dimensions used for the test section of the sub-size specimens were a length of 1.2 in (3.048 cm), a width of 0.25 in (0.635 cm), and a thickness of 0.038 in (0.97 mm). The dimensions used for the test sections of

the full-size specimens were a length of 2.5 in (6.35 cm), a width of 0.5 in (0.27 cm), and a thickness of 0.084 in (2.13 mm). The weld parameters and channel design for embedded FBG sensors were identical to that used for regular optical fiber.
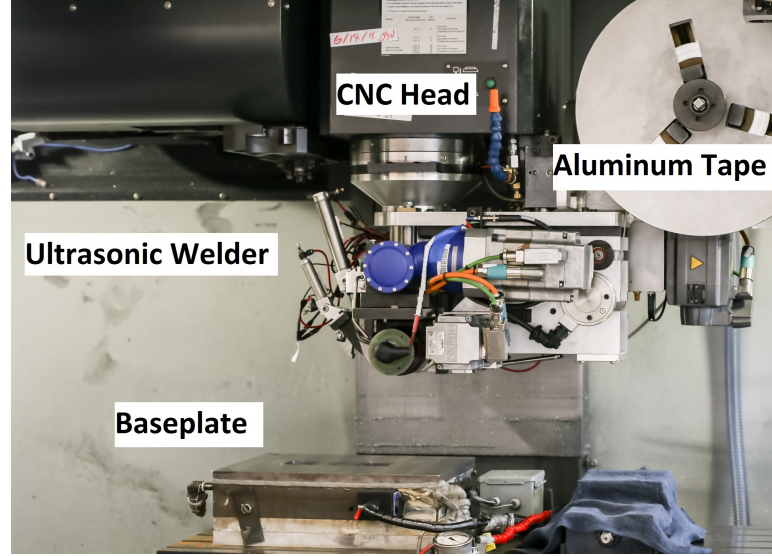
Figure 2.2: Commercial 9 kW UAM system, Fabrisonic SonicLayer 4000.

2.2 Optical Testing

Four major optical phenomena were examined during this study, which were core survival during embedment, birefringence as a result of cross-sectional deformation during embedment, peak wavelength shifting during mechanical/thermal testing, and incsription reversal of the grating. Due to the small size of the optical fiber, excessive load on the fiber itself can easily result in brittle fracture and failure. Since the transmission of data to and from the interrogator and grating requires the core of the fiber to be intact, core survival was the first priority in sample fabrication.

Previous studies used electroplated fibers to encourage bonding between the coating and matrix, as well as to provide additional protection to the fiber. Since part of the goal of this study was to use commercially available fiber and avoid the introduction of additional/unnecesary steps in the fabrication process, samples were built with a precut channel. Figure 2.3 shows how the loading on the fibers changes during the weld process as a result of pre-placement channels. This use of a channel prior to encapsulation will be referred to as embedding in an unloaded configuration, as the fibers themselves were not mechanically loaded by the down force from the sonotrode.
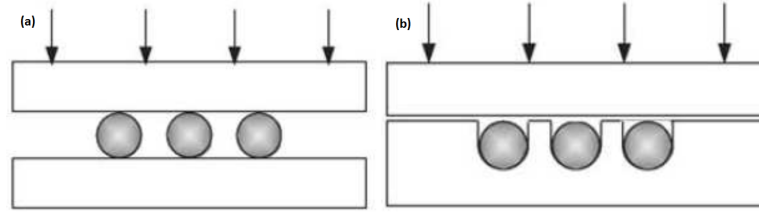
Figure 2.3: Embedded fiber configurations: (a) loaded configuration; (b) unloaded configuration with channels

Birefringence is a measure of the dependence of the coefficient of refraction to the orientation of the material [3]. In terms of sensor performance, a fiber with a 'poor' birefringence response was one in which the reflected wavelength is dependent upon the polarization of the incoming light. Heavily birefringent FBGs have a large amount of noise due to this dependence, and are undesirable. Birefringence is caused by the cross-sectional deformation of the fiber [12], and part of this study involves minimizing birefringence through sample geometry design. A fiber with a perfectly circular cross section will exhibit no birefringence. In the case of applications in

which fiber channel design is either limited or not possible, there are types of optical fiber in which birefringence is induced, and kept constant, that could be used as well. Birefringence testing was performed using a polarization controller. The polarization controller functions by inducing a cross sectional change along parts of the fiber between the interrogator and the FBG, shown in Figure 2.4. This allows for a spectrum of arbitrary polarization to enter and exit the FBG, providing a wide range of reflected data. A threshold value of 15 pm of noise was used to quantify 'good' birefringence performance of FBGs. Figure 2.5 shows an example of a heavily birefringent fiber, and how the accuracy of the strain signal is lowered.
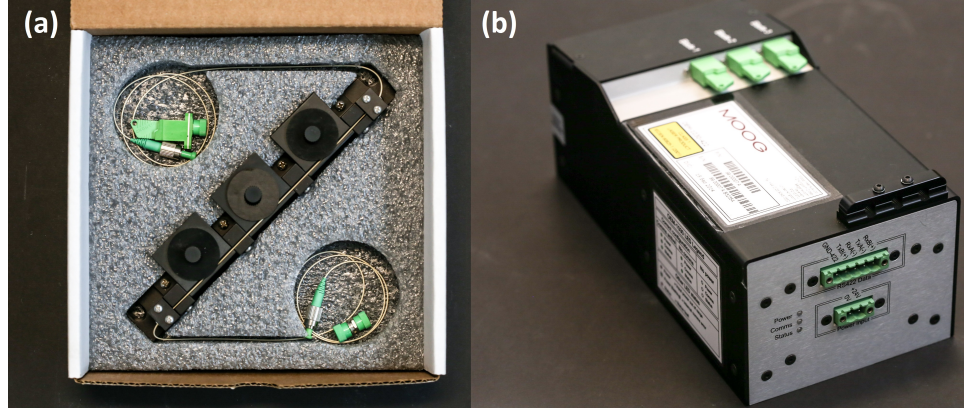
Figure 2.4: Fiber Bragg grating test equipment: (a) polarization Controller (b) FBG interrogator.
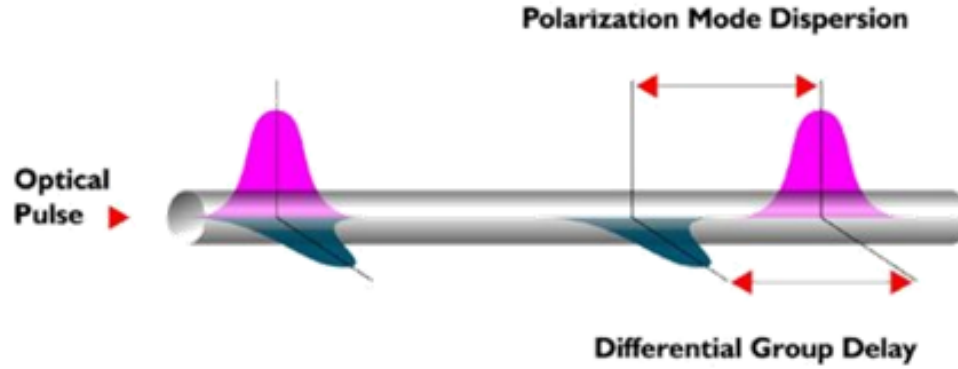
Figure 2.5: Physical representation of the impact of birefringence on a optical signal.

Peak wavelength shifting refers to a method of detecting non-uniform sensor loading. When the sensor is subject to non-uniform loading, the distances between gratings are no longer consistent, and a number of different wavelengths begin to resonate within the sensor. This leads to the distortion of the reflected light profile, and as this distortion increases it is possible to see the formation of multiple peaks within the reflected data. If the overall maximum is suddenly overtaken by a different local maximum, an interrogator that only reads the wavelength with the largest amplitude will exhibit a 'hopping' in the data, such as is the shifting shown in Figure 2.6. This type of reflected profile distortion occurs in two common cases: firstly, when the embedded length is not sufficient to eliminate shear lag from the matrix to the sensor, and secondly when the sensor is subjected to a dynamic loading that causes a deformation gradient within the sample. Although the absence of peak wavelength shifting is not sufficient to guarantee that no profile distortion is taking place, the

presence of peak wavelength shifting within a dataset confirms non-uniform loading on the sensor, thus test conditions that eliminated wavelength hopping were used.
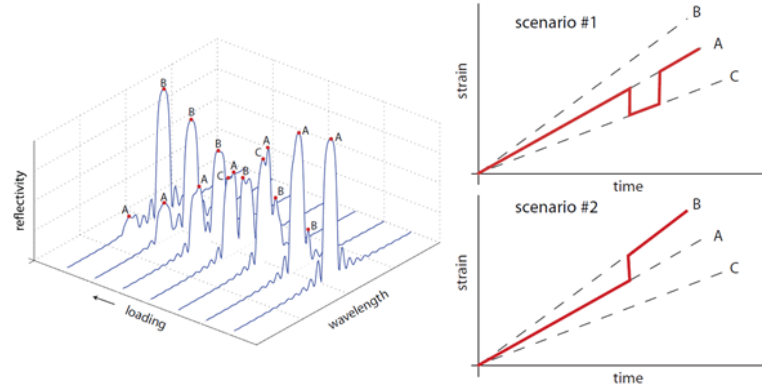
Figure 2.6: Graphical representation of peak wavelength shifting

Inscription reversal is an effect which can occur at high temperatures where the grating begins to disappear. This effect is based on the temperature at which the FBGs themselves were written, information that was not accessible during this study. The effect is characterized by the loss of signal after some time at too high of a temperature.

Samples of bare fiber as well as FBG specimens after testing were also subjected to microscopy. Samples were cut using a diamond bladed saw in order to preserve the cross sectional surface, and were then mounted onto bakelite. The samples were then sanded using a belt sander, and then polished using stages of sanding up until 0.05 μm silica as a final polishing stage. These samples were then observed under an optical microscope, and were back-lit using a flashlight when appropriate. Bare fiber was observed through mounting in epoxy in certain cases. Microscopy was performed

to investigate core survival, coating deformation, and the effects of high temperature loading on coating.

2.3 Mechanical Testing

Test specimens were connected to the interrogator after fabrication, and subject to manual loading to ensure sensor survival and mechanical coupling. Mechanical characterization was then carried out in the form of tensile loading and cantilever bending tests. All FBG measurements were taken through an interrogator supplied by Moog Inc, which exported analog data to an NI DAQ unit through the use of a digital to analog converter circuit. This was done to ensure that all values were measured on the same time signal, allowing for direct comparison of strain, temperature, and tensile load values. Figure 2.7 shows one of the tensile test setups.
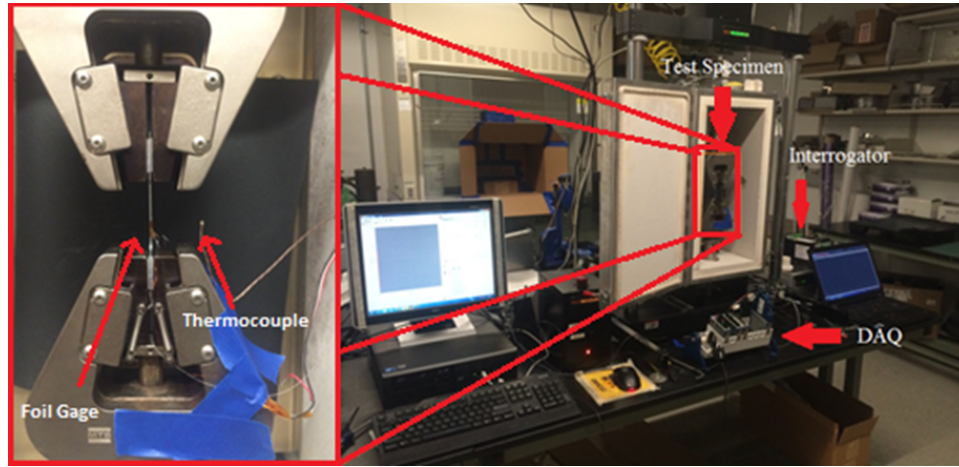
Figure 2.7: Tensile testing: load frame with temperature chamber and gripped test specimen.

2.3.1 Low Temperature Tensile Testing

The dogbone test specimens were designed according to ASTM standards for testing the tensile strength of materials. The geometry is such that tensile stress is concentrated within the small width test section of the sample, and the FBG is placed in the center of the specimen. Tensile loading was accomplished using both an MTS load frame with integrated furnace and a test resources load frame with integrated thermal chamber. Quasistatic cyclic loading was performed to investigate the repeatability of tests and to look for evidence of hysteresis in the sensor profile. The quasistatic load profile used consisted of driving the grips, which held the specimen, at a rate of 0.010 in/s (0.254 mm/s) until a load of 50 lbs (222 N) was observed, and then unloading at the same rate until a load of 5 lbs (22.2 N) was observed. Given the geometery of the specimens, the expected maximum loading within the test section was approximately 5221 psi (36 MPa), well below the yield threshold for bulk 6061 aluminum of 34800 psi (240 MPa). Failure testing was performed to determine maximum sensor load threshold. The loading rate was kept the same as in previous tests, but given a threshold value of 500 lbs (2220 N). Given the sample geometry, bulk aluminum 6061 would be expected to break at a tensile loading of approximately 400 lbs (1780 N). The sampling rate for the load/displacement was 250 Hz for these tests. The FBGs were measured using an interrogator supplied by Moog Inc, which exported analog data to a National Instruments data acquisition unit.

2.3.2 Cantilever Bending

Cantilever bending testing was performed to investigate the dynamic response and bandwidth of the FBG sensors by clamping a specimen at one end and inducing

bending. Two types of bending test were carried out, the first being a manual cyclic loading of the sample in order to ensure real time strain data was being obtained and correlated with the data measured by the foil gage. Due to the sensors' proximity to the neutral axis, shown in Figure 2.8, the data was scaled so that the strain profile was more visible. Manual quasi-static bending was induced in the sample, as well as a flick test to obtain the impulse response. The second bending test involved flicking the sample to obtain the impulse response. Frequency response analysis was carried out during this second test to compare the resonant frequencies observed by both sensors. Vishay foil strain gages were mounted on the surface of test specimens using epoxy, and were used as a comparative benchmark for sensor performance. The foil gages that were used to examine the effects of thermal loading on embedded FBG performance have a coefficient of thermal expansion (CTE) consistent with that of aluminum, and the strain data measured was not sensitive to temperature changes.
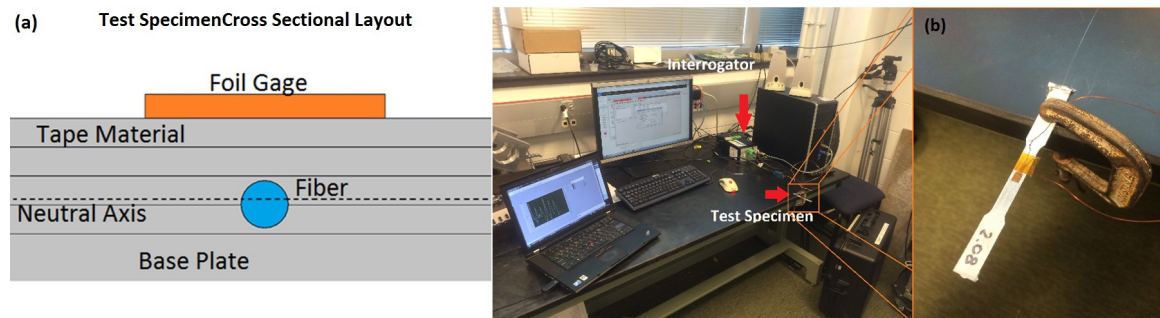
Figure 2.8: Cantilever testing: (a) test specimen cross section; (b) cantilever test setup for flick testing.

2.4 UAM Process Monitoring

FBG sensors were used to take measurements during the UAM process itself. Although the UAM process is known to be low temperature and induce high amounts of deformation at the interfaces of the tape and structure, the exact temperatures and strains are difficult to measure. As a result, the exact physical cause of bonding in ultrasonic welding is not fully understood. By performing in situ testing, it is possible that more data about the state of the material during bonding can help shed light onto the process itself. In other cases where a thermally sensitive material is being embedded, it is also valuable to have an idea of what temperatures are to be expected based on the location of the material relative to the sonotrode. Additionally, in-process interrogation of the FBG sensors can help to determine in real time if a sample is successfully constructed. The sample geometry used for UAM process monitoring was the same geometry used for tensile test specimens, shown in Figure 2.9.

Figure 2.9: Test specimen being manufactured with FBG placed into channel

Both acrylate and polyamide coated FBG sensors were embedded into aluminum 6061, and data was taken for 1 layer builds, 2 layer builds, and a 'roll' pass in which the horn was passed over the specimen without active ultrasonics. The acrylate coated FBG measured a compressive loading of the sample followed by a tensile loading, which was to be expected as the horn approaches and then passes the FBG within the specimen. There was a rapid decay after the weld, which was consistent with a decaying temperature of the sample. After the temperature had decayed to a level near room temperature, the measured strain was different from the initial nominal strain value, indicative of an induced strain change within the FBG. This could be due to plastic deformation and flow of the matrix material during welding, which would explain the lack of an induced strain change during the 'roll' test. Due to a circuitry error, some of the profiles do not have data regarding compression. Figure

2.10 shows the UAM test setup with sensors and data acquisition equipment used during welding.
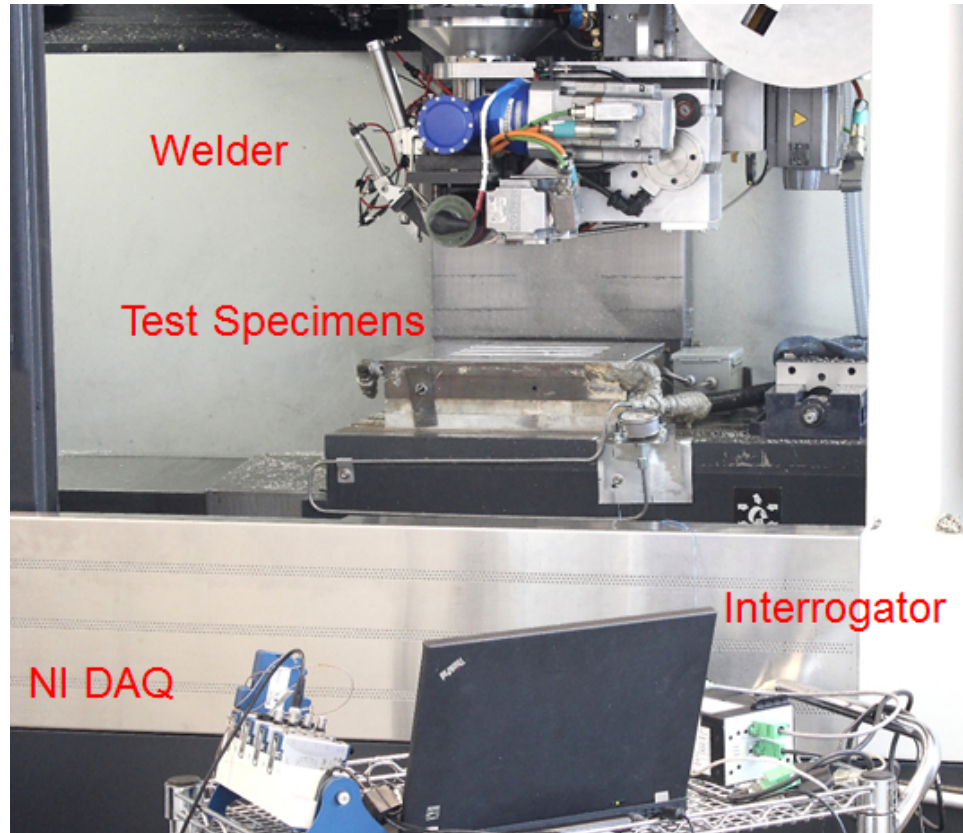
Figure 2.10: SonicLayer 4000 with requisite circuitry for in-situ FBG sensing.

2.5 High Temperature Testing

Samples were heated in an oven while under no mechanical load in an effort to obtain their maximum operating temperature. FBG strain data was collected and compared to the CTE of aluminum. The inital goal of the maximum temperature test was to obtain a temperature at which the CTE of the aluminum and FBG diverged,

as divergence would imply the loss of interfacial coupling between the aluminum and sensor. It became apparent during testing that no such divergence occurs with UAM embedded FBGs, and the purpose of the test became to verify the internal temperature through the use of an embedded thermocouple. After internal temperature verification, the coating of the embedded sensor was investigated for signs of degradation. Temperature measurements were taken in real time from K-type thermocouples.

2.5.1 Oven/CTE

Oven testing was intended to find out the maximum operating temperature of the embedded FBG sensors, as well as shed insight towards their CTE. The limitations of taking measurements in a thermally dynamic environment were explored. Lastly, the effects on the protective coating material of the FBGs at high temperatures were investigated. Figure 2.11 shows the schematic for oven testing.
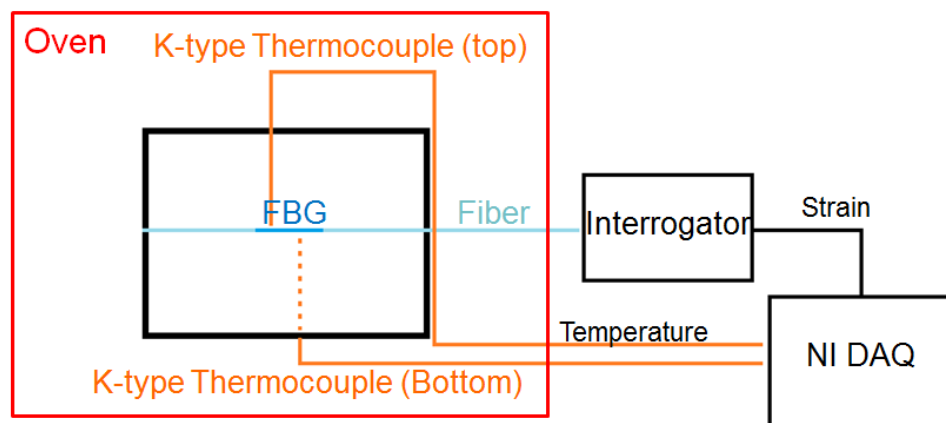
Figure 2.11: test setup used for examining embedded FBG CTE.

2.5.2 Elevated Temperature Tensile

High temperature tensile testing was performed on an MTS load frame with integrated furnace. The samples were gripped in place and loaded at a rate of 0.1 in/m (2.54 mm/m) until a load of 1000 lbs (4450 N) was measured, held at max load for 10 seconds, then unloaded at the same rate until a tensile load of approximately 0 was measured. During a temperature set point change, the sample was held by the grips and not subjected to a changing mechanical load input until a few minutes of time had passed for the ambient temperature to settle. No foil gages were used to obtain redundant strain data, as the ambient temperature exceeded the operating temperature of the epoxy used to secure the foil gages to the samples. Temperature measurement was accomplished through the use of four separate thermocouples placed in the furnace. The load frame with integrated furnace and data acquisition is shown schematically in Figure 2.12
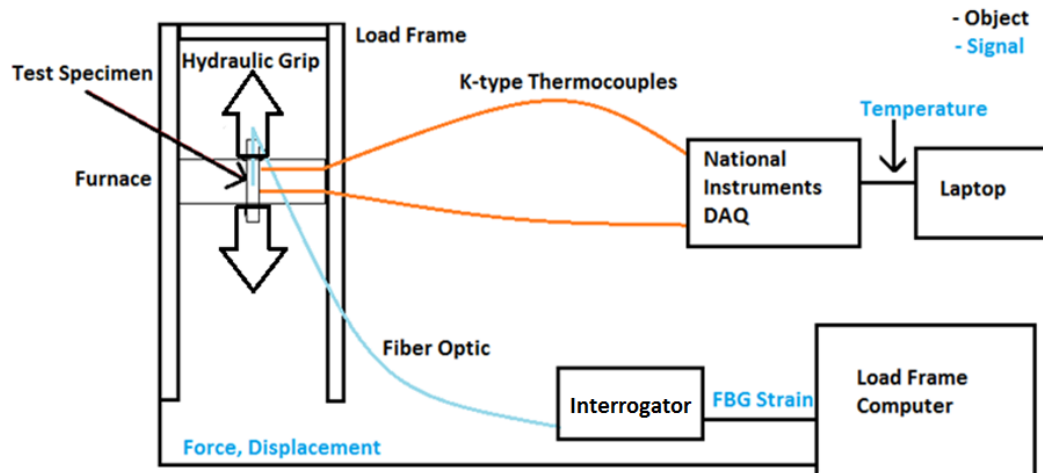
Figure 2.12: Schematic for high temperature tensile testing.

Chapter 3: RESULTS AND DISCUSSION

3.1 Optical Testing

Core survival was verified through cross-sections of UAM built specimens with optical fiber, in coated as well as uncoated cases. Birefringence effects were found to be mitigated through 'unloaded' specimen fabrication, and found to increase as the number of welded layers increased. These findings were consistent for both acrylate and polyamide coated FBGs. Inscription reversal of the FBG gratings, an effect that can occur when the temperature exceeds the temperature at which the grating was written, was not observed at any temperatures.

3.1.1 Microscopy

Figure 3.1 shows the preliminary micrographs taken to confirm core survival and examine coating deformation. Dual acrylate coated single mode fiber (without grating) was first examined. The impact of channel depth on deformation of the protective coating of fibers was inspected for dual acrylate coated fiber, and it was found that deformation was minimized with a channel depth approximately equal to the diameter of the fiber at 0.010 in (0.254 mm). When the depth was larger, 0.011 inches, the coating was deformed and pushed above the glass, and when the depth was smaller,

0.009 in (0.229 mm), the coating was deformed along the interface. This led to the

typical sample channel depth being chosen as 0.010 in (0.254 mm).
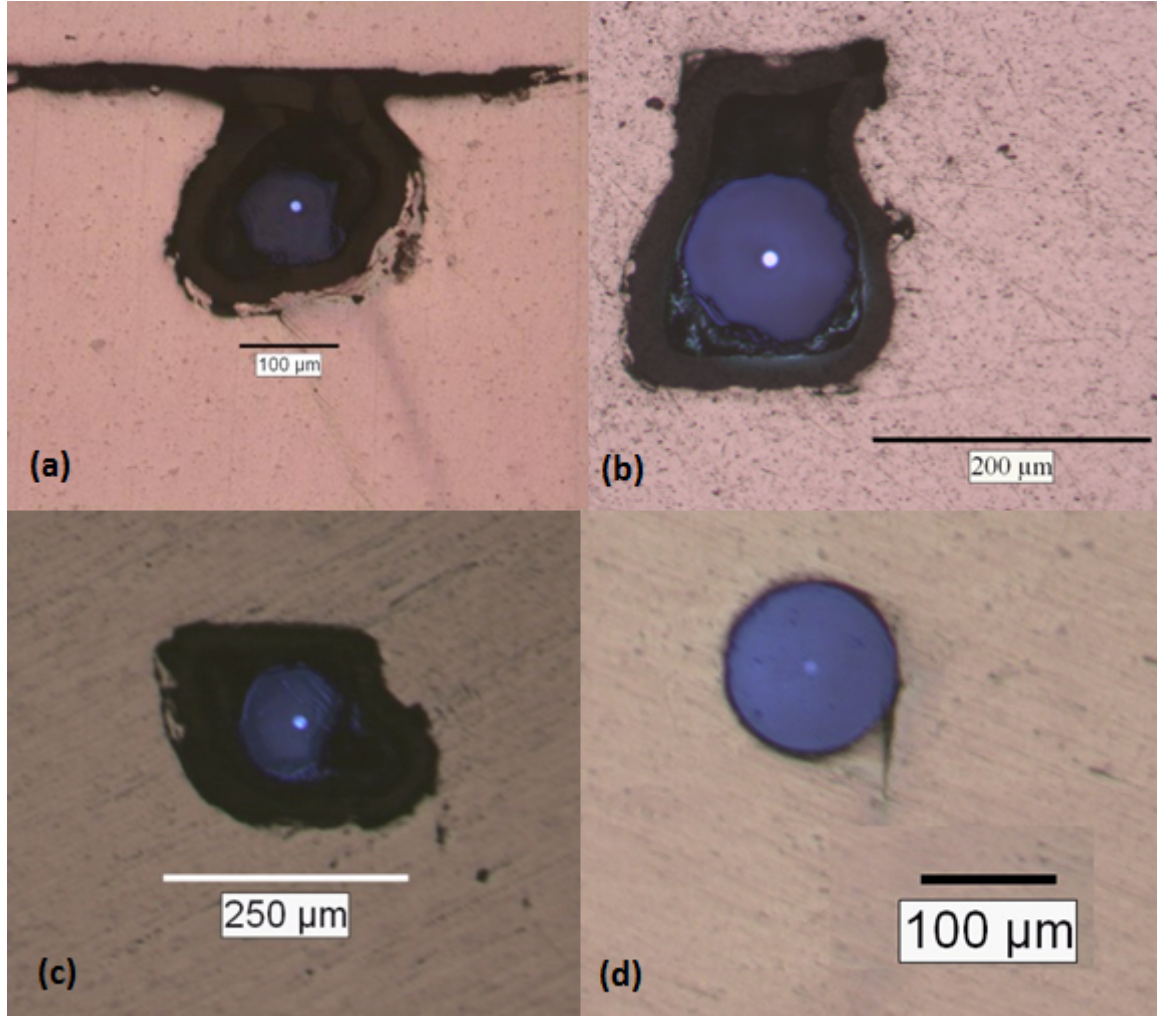
Figure 3.1: Embedded optical fiber (without grating) backlit to showcase core survival: (a) acylate coated fiber in 0.009 inch channel, clear contamination of weld interface by coating material after embedment; (b) acrylate coated fiber in 0.011 inch channel, coating deformed upwards into channel; (c) acrylate coated fiber in 0.010 inch channel, deformation minimized; (d) stripped fiber embedded, core verified and no obvious deformation of glass cladding.

Figure 3.2 shows polyamide coated fbgs that were examined immediately after embedment and also after mechanical testing. While polyamide coated FBGs showed little difference to acrylate coated fiber prior to testing, clear deformation of the coating was shown when samples were pulled to failure. This deformation of the coating suggests that loading imparted into the aluminum was not consistent with the loading observed by the coating, a result confirmed in strain tracking experiments which revealed slip occurring at the aluminum and coating interface.
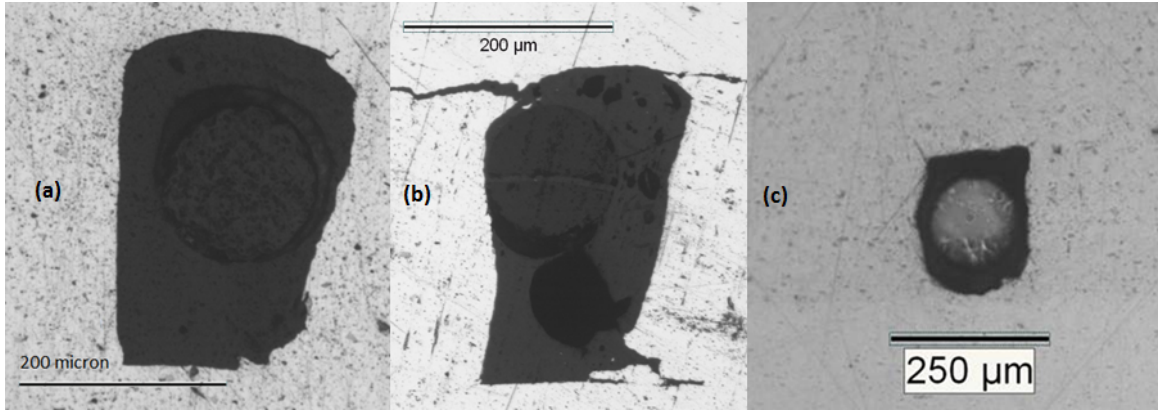
Figure 3.2: Embedded polyamide coated fiber: (a) fiber located within the test section of a specimen pulled to failure, deformation of the fiber indicates that the channel deformed along its depth; (b) opposite side of the cross section from part a; (c) FBG cross section taken after building without any testing, no abnormal deformation present.

3.1.2 Birefringence

For this study, the birefringence was investigated by use of a polarization controller, which served to send a wide range of polarized signals into the fiber to induce noise. A 'poor' FBG with cross sectional deformation was supplied by Insensys and

used as a reference, characterized by a total shift in Delta Wavelength of more than 0.06 nanometers when a polarized signal is passed through the mechanically unloaded FBG. This shift corresponds to an uncertainty of more than 60 microstrain during measurements. No significant birefringence effects were experienced by the fiber when embedded with proper channel height. When the FBGs were placed in a loaded configuration, they saw an increase in losses due to birefringence, regardless of the type of external protective coating. Conversely, utilizing a channel to embed unloaded fiber in all cases minimizes the birefringence. FBGs embedded in the unloaded configuration often saw less than a 0.01 total wavelength change in response to polarized light, compared to the reference 0.06 bad sensor response as shown in Figure 3.3. FBGs embedded in a curved configuration also saw no change in birefringence response.
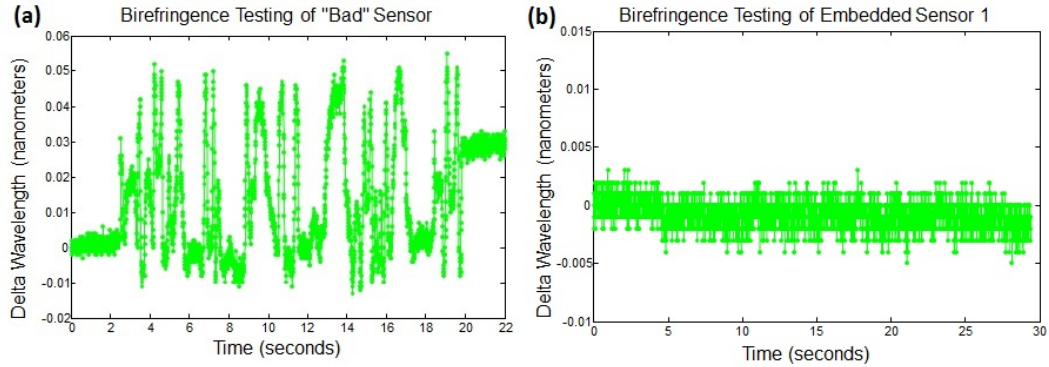
Figure 3.3: Response to polarization of FBGs: (a) Reference 'poor' sensor supplied by Insensys; (b) Acrylate coated sensor after embedment into aluminum.

3.2 Strain Tracking

The first embedded FBGs were characterized in terms of their ability to accurately measure the strain observed in the aluminum samples in which they where built. This took the form of profile matching, value matching, and dynamic tests for both acrylate and polyamide coated FBGs whose optical properties were verified by birefringence testing prior to physical testing. Reference strain measurement was accomplished using vishay brand foil strain gages, externally mounted on the test specimens at the same location as the FBGs. The initial cantilever testing data shown in Figure 3.4 confirmed profile matching, and showed a downwards drift in strain measurement as a result of temperature increasing during the test as the sample was pressed upon manually. As a result of the FBG being located very closely to the neutral axis of the sample, this data was scaled using a mathematical factor, and the values shown for the FBG sensor are not the actual values measured. In tensile testing, the strain values measured by the foil gage were matched with the FBG measurements.
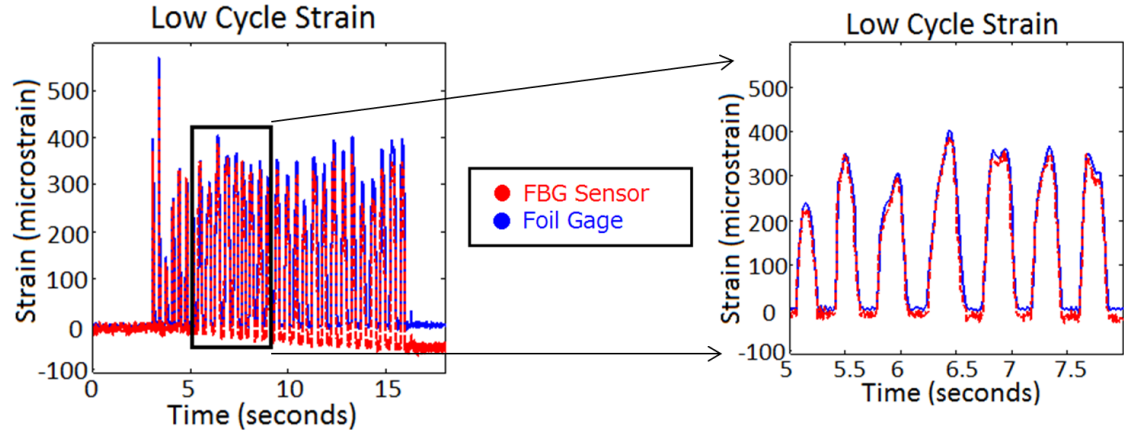
Figure 3.4: Cantilever testing: (a) scaled data showing drift on the FBG measurement due to the changing temperature; (b) load profile matching via zoomed in data.

Flick testing revealed that the FBGs were able to obtain the harmonic frequencies of the specimens when subjected to impulse bending conditions. These frequencies were measured in the foil gage values, although in both tests a lower frequency term was observed in the FBG values. This lower 'phantom' frequency was likely a result of noise within the FBG interrogator, as there is no built in anti-aliasing. The results of the cantilever dynamic testing are shown in Figures 3.5 and 3.6.
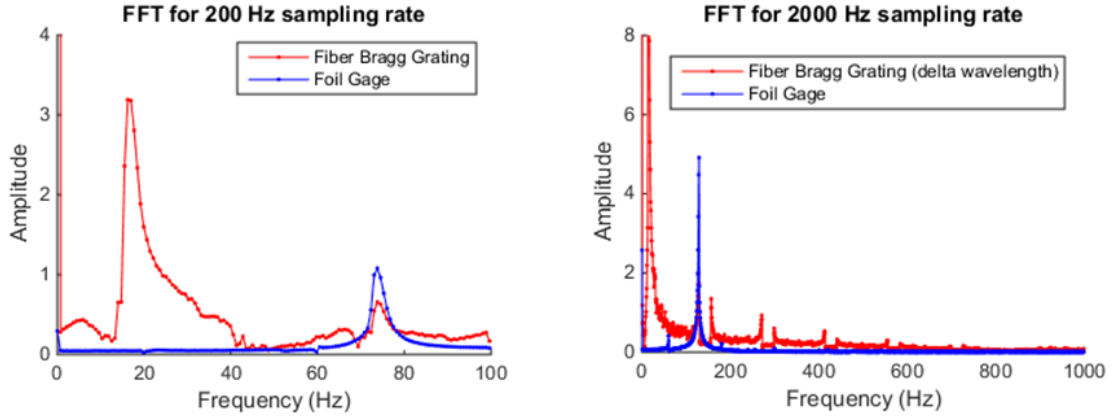
Figure 3.5: Cantilever testing: (a) 200 Hz sampling rate frequency response function (FRF); (b) 2000 Hz FRF. Note the prescence of an additional low frequency peak for the FBG data that is not present in the foil gage data.
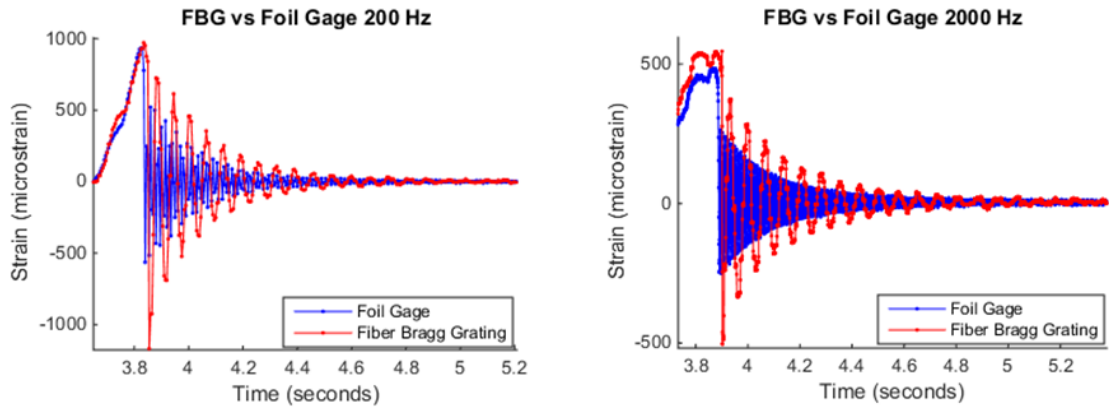
Figure 3.6: Cantilever testing: (a) 200 Hz sampling rate data; (b) 2000 Hz sampling rate data.

3.2.1 Acrylate Coated FBGs

The acrylate coated embedded FBGs showed clear profile and value matching with the foil strain gages. Both quasi-static cyclic loading at loads under the yield point of aluminum and load-to-failure tests showed little disagreement with the surface gages, as shown in Figure 3.7. The FBG sensors were able to transmit data up until the point where the aluminum matrix failed, which caused the fiber to fail simultaneously. The slight differences can be accounted for by the fact that the surface gage and internally placed FBG can expect to see slightly different loads, as well as slight shifts in terms of temperature over the course of testing. Thermally invariant foil gages were used for the reference measurements, which meant that as the temperature shifted the FBG measurement changed relative to the foil gage. Tests where this temperature induced shifting took place are clearly observed when the temperature values (taken by externally mounted K-type thermocouples) are superimposed over the strain vs time plots.
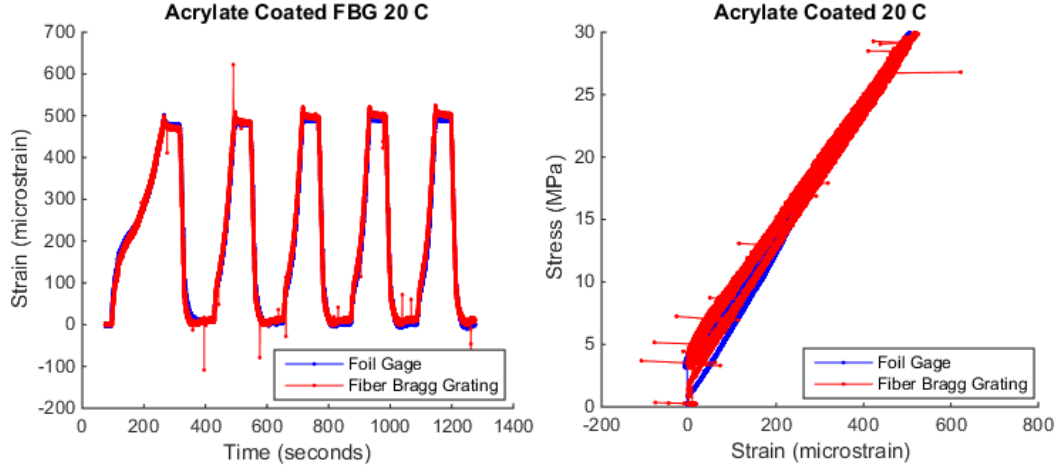
Figure 3.7: Acrylate coated FBG compared with foil gage during quasi-static room temperature tensile testing.

At room temperature, the FBG strain profile matched almost perfectly with the foil gage profile during low tensile load quasi-static cyclic loading. Additionally, the loading/unloading curves of the stress/strain profile during cyclical loading were approximately the same, which was consistent with the expectation of no hysteresis type behavior during non-yielding loading. Figure 3.8 shows agreement between the foil gage and FBG data during fail testing. Figure 3.9 shows the 70 C cyclic tensile testing data, and there appears to be an upwards shift evident on the FBG data as time progresses. This data was explained when looking at the exact temperature profile during the test. Since the temperature varied in a step-like progression, the strain data was offset in kind. Both the foil gage and FBG were able to return to their nominal strain value at the end of each cycle, which confirmed that the acrylate coated FBGs were able to obtain consistent results.
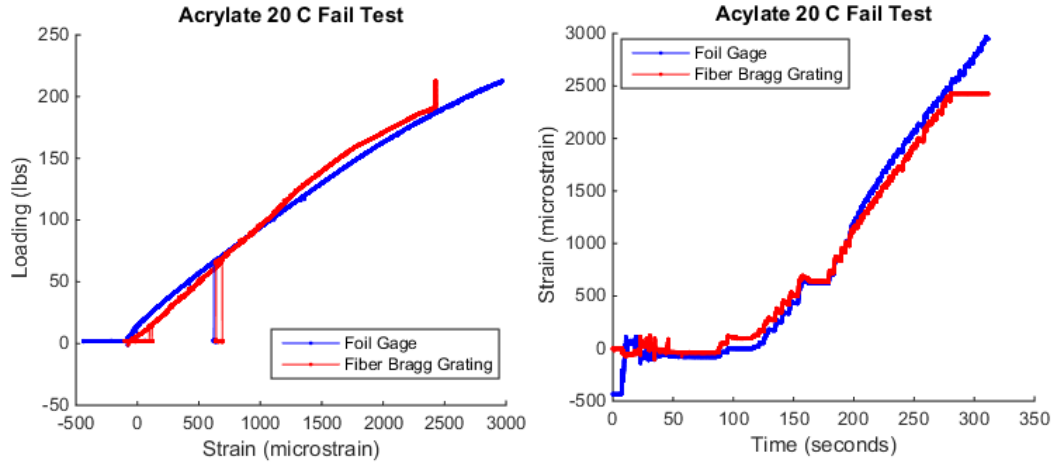
Figure 3.8: Acrylate sensor subjected to maximum loading test. Interrogator wavelength limit was reached prior to sample failure, good agreement between strain values during test.
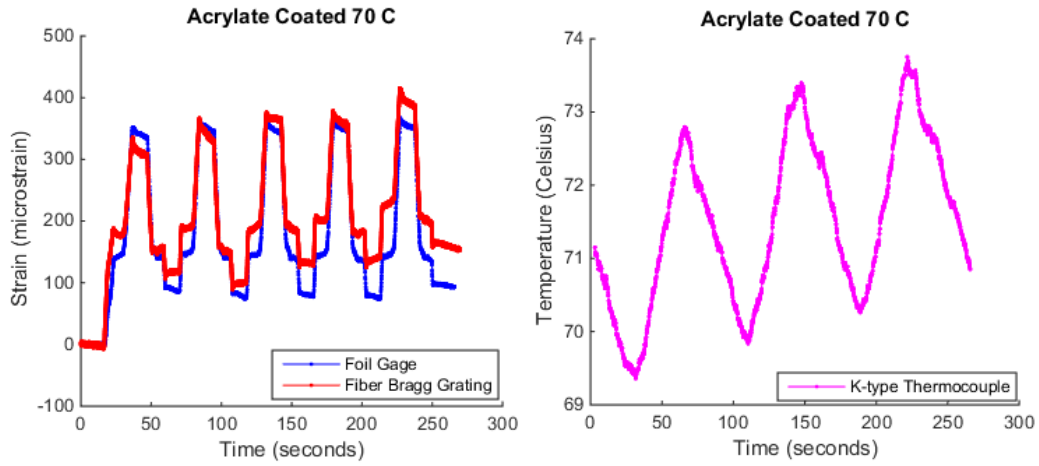
Figure 3.9: strain data comparison at 70 degree Celsius set point.

3.2.2 Polyamide Coated FBGs

Polyamide coated FBG sensors were not able to track either the quasi-static cyclic loading or yield profiles of the specimens as accurately as shown in figures 3.10 and 3.11. In cyclic loading tests, evidence of hysteresis appeared in the form of the loading/unloading curves not matching up, and in yield loading tests no evidence of yield was observed. These results in conjunction suggested that slip was occurring between either the polyamide and aluminum, or between the glass and polyamide, as some manner of inconsistency was present between the FBG output and aluminum matrix state. Slippage between the aluminum matrix and polyamide coating was seen in Figure 3.12, where the aluminum matrix was observed to have failed around the fiber during failure testing. The FBG shown in this figure was still functional and outputting a signal after failure of the matrix.
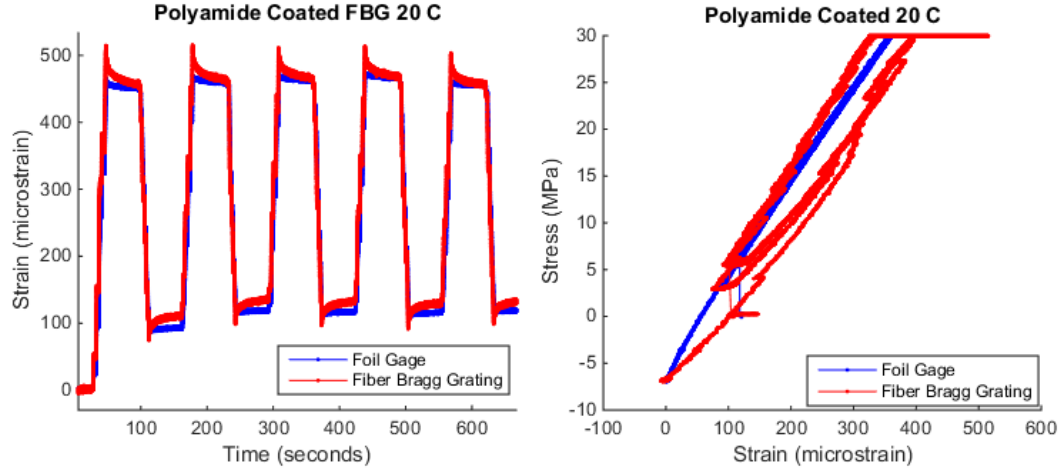
Figure 3.10: Cyclic tensile testing of embedded polyamide coated FBG. The data on the left shows a time dependence on the measured strain in terms of changing measurement during the portion of the load profile in which no change in load is occuring (plateaus on the foil gage profile), and the data on the left shows departure between the loading/unloading profile for the FBG that wasn't present in either the foil gage or the acrylate coated FBGs.
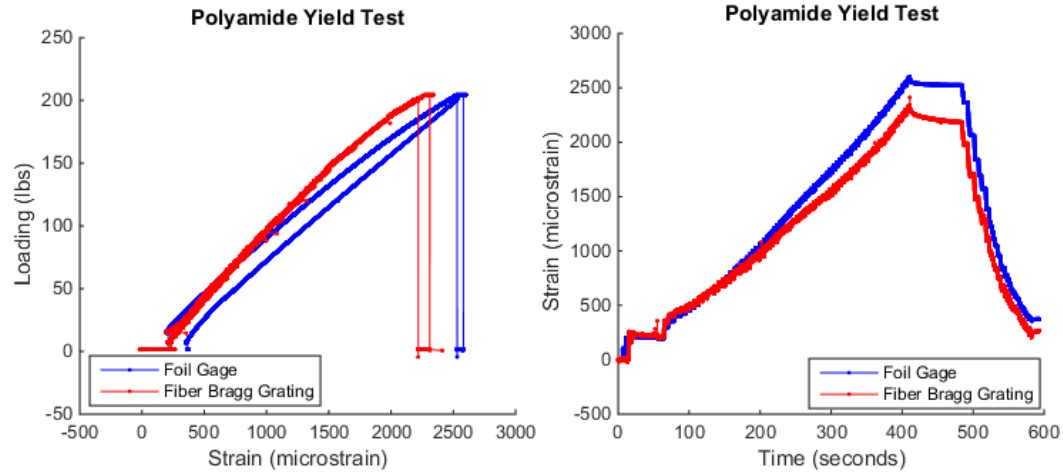
Figure 3.11: The FBG load/strain profile is consistent during both loading and unloading, whereas there is clear evidence of yielding in the foil gage measurement.
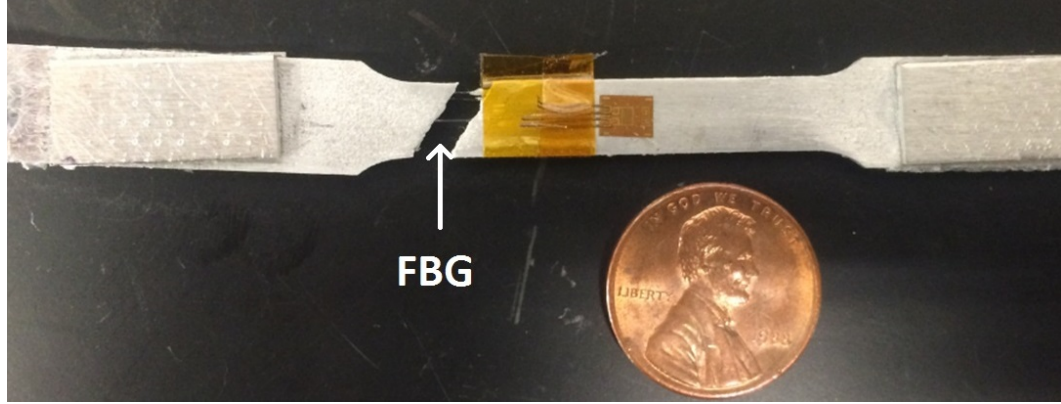
Figure 3.12: Polyamide coated sensor surviving despite failed aluminum matrix. This is definitive evidence of interfacial slip.

3.3   UAM Process Monitoring

The successful validation of FBG strain tracking as a result of being embedded via the UAM process allows for a potential new method of performing in-situ monitoring during UAM. This was accomplished by interrogating the sensors during welding. Some issues with obtaining meaningful strain measurements through FBG measurements exist, mostly as a result of the relative speed of UAM. Since the interrogator was not designed for high speed sensing, it was not possible to obtain data at the ultrasonic frequencies used to drive the welder. Additionally, the speed at which UAM occurs in conjunction with the relatively thin contact area mean that FBGs do not experience a perfectly uniform loading when the horn rolls over the fiber. FBGs are also unable to measure transverse loading, and as such cannot provide insight into the vibrations induced upon a welded part. Since FBGs are temperature sensitive, an additional temperature measurement must be taken in close proximity to the FBG, either in the form of a thermocouple, IR image, or some other method. Figure 3.13

shows some embedded thermocouple data taken during welding. Lastly, due to the requirement for a consolidating layer of tape placed over the sensor in order to fully encourage bonding, limited insight can be provided in regards to surface level effects.
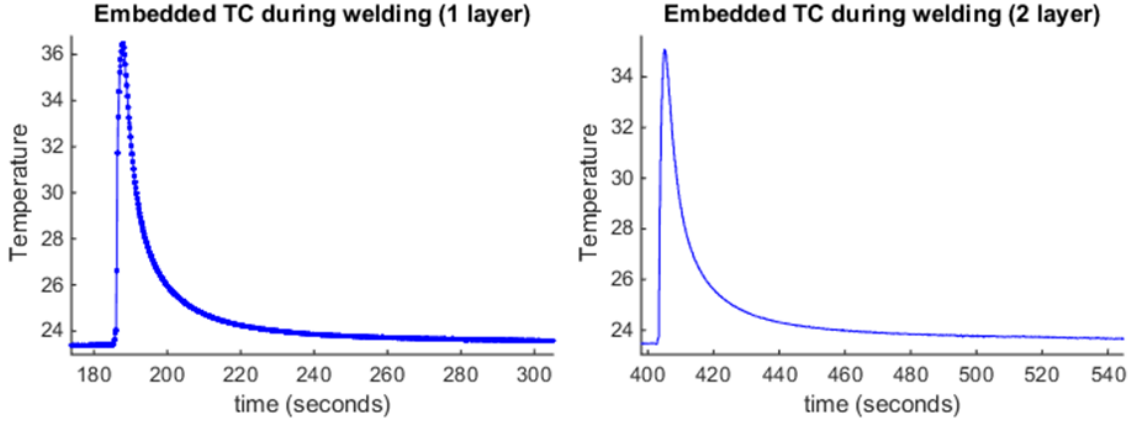
Figure 3.13: Temperature data obtained by embedding a K-type thermocouple in a channel prior to welding. This temperature sensor is located at approximately the same z-location as the embedded FBG, and should capture a similar thermal measurement.

A fairly consistent strain profile is observed by the acrylate coated FBGs during weld monitoring in Figure 3.14. Firstly, a compressive loading is induced upon the FBG as the horn approaches the FBG. Second, a drastic shift from compression to tension occurs the horn passes over the sensor. A rapid decrease in strain signal followed by a gradual decay occurs, consistent with alleviated mechanical loading on the UAM part and thermal decay towards room temperature. After a cooling time of over 100 seconds, the thermal decay has mostly stopped, and a new nominal strain value was observed. This was likely a result of plastic deformation induced within the aluminum matrix at the foil interface. This was supported by the lack of nominal

strain shift during passes where the ultrasonic transducers were not driven, and the horn was only rolled over the sensor. Lastly, this nominal shift was not standardized, and could be in either the tensile or compressive direction. Since neither the bonding mechanism nor deformation profile of UAM are perfectly understood, it is unclear whether or not this residual strain change is uniform over the sensor.
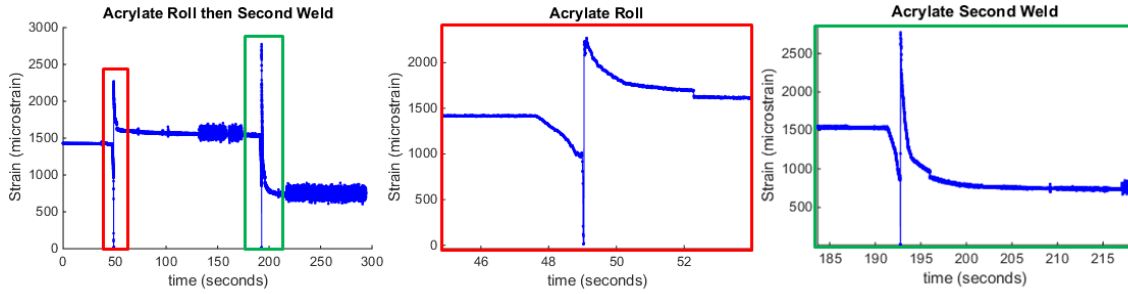
Figure 3.14: Roll and weld profile of FBG during UAM: there is not a substantial nominal strain shift during roll, and there is a quantifiable change within the weld pass. A compressive and subsequent tensile load are present in both profiles.

The profile exhibited by the acrylate coated FBGs is not consistent with the load profile observed by the polyamide coated FBGs in Figure 3.15. Although the first weld exhibited signal decay, issues with the measurement meant that thermal decay could not be seen. Since worse coupling is to be expected in the polyamide coated case, the effect of thermal loading on the sensor was not clear. The sensor also failed during the second layer weld, which may have lead to the erratic profile shown. If nothing else, this set of tests confirmed the ability of the interrogator to check for sensor survival in real time during sample fabrication.

47
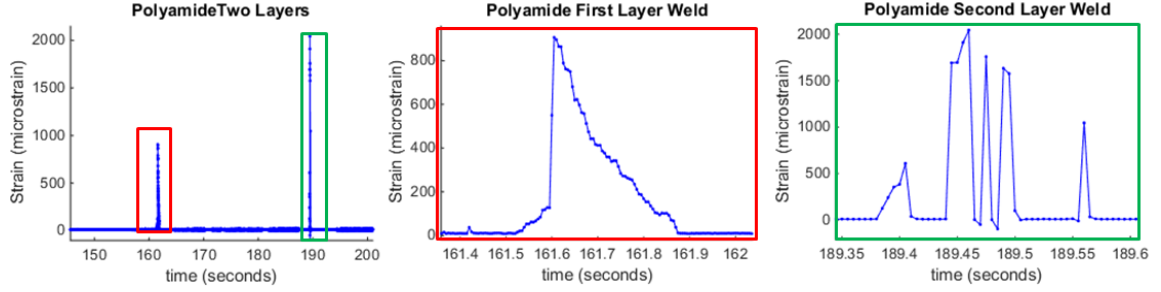
Figure 3.15: First and second weld passes over polyamide coated FBG: Compressive loading was not observable due to setup error, but a comparatively slight ramp of the strain signal prior to a larger jump was observed. The erratic jumping of the strain signal during the second pass may correspond to optical issues with the fiber as it failed. The sensor failed within the build, not at the fiber exit point.

3.4 High Temperature Testing

Initial high temperature testing was done using a sample configuration in which the fiber ran throughout the length of the entire test specimen. Since the hot zone of the test was limited to approximately an inch beyond the test section of the samples, mechanical coupling between the acrylate and aluminum within the grips of the load frame, which were thermally isolated from the hot zone, was assumed. In spite of this external coupling, the modulus of elasticity of aluminum was confirmed by sensor data in Figures 3.16 and 3.17, which supported the conclusion that the gratings were not subjected to inscription reversal and were functioning normally.

48
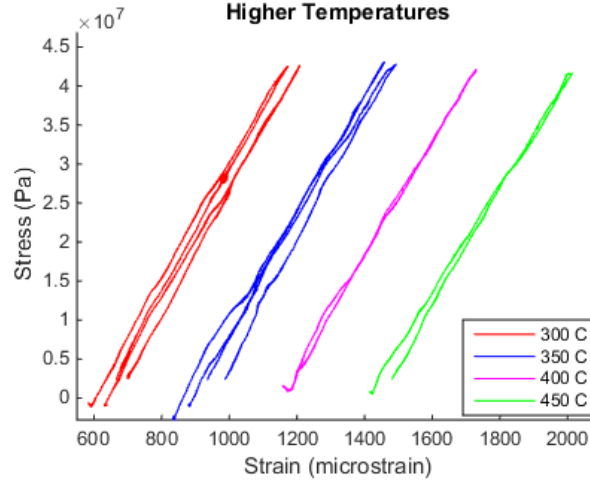
Figure 3.16: High temperature testing: the slope of the stress strain curve matches well with the modulus of elasticity of aluminum (approximately 67 GPa).
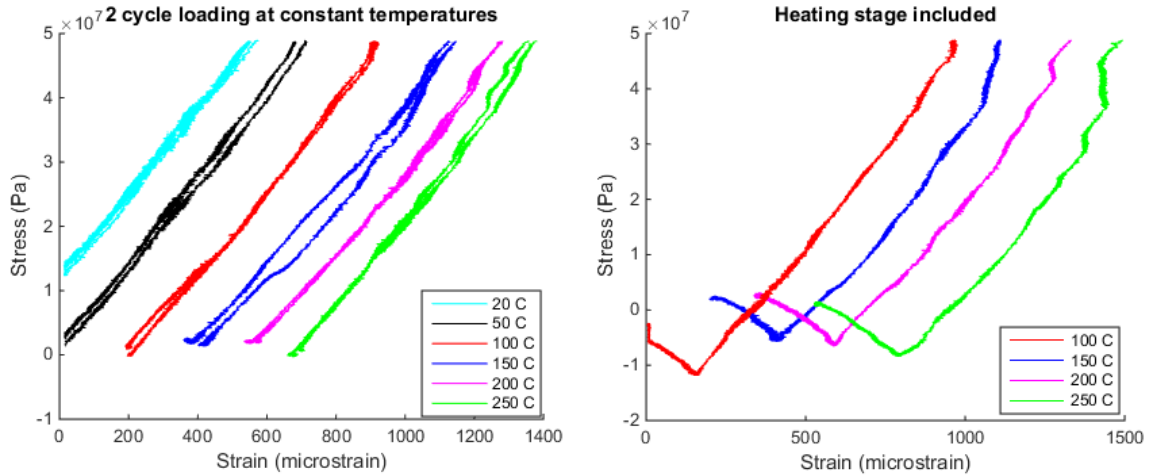
Figure 3.17: Temperature testing: the slope of the stress strain curve matches well with the modulus of elasticity of aluminum (approximately 67 GPa). During the heating stage, no loading signal was given to the load frame. As a result, the thermal expansion counteracts the tensile loading on the part, inducing a compressive load onto the test specimen.

Acrylate coated FBG sensors were chosen for high temperature characterization due to the lack of slip observed in room temperature tensile testing. FBG sensors showed no sign of inscription reversal, the shift in wavelength and reflectivity accelerated above the annealing temperature of the FBGs, during high temperature testing. This was confirmed by the fiber strain signal accurately tracking the modulus of elasticity of aluminum during testing up to 550 degrees Celsius. The results are shown in Table 3.1.

Table 3.1: Maximum strain values and modulus from high temperature measurements

Temperature (C)	Maximum Strain(microstrain)	Elastic Modulus (GPa)
20	576	66.7
50	717	67
100	925	63.7
150	1149	63.8
200	1280	63.2
250	1380	66.8
300	1209	76
350	1494	73.5
400	1732	73.9
450	2015	70

Despite the accurate modulus tracking, the samples were designed such that fiber ran through the length of the entire sample. This enforced mechanical coupling between the fiber in the grips of the load frame, well outside of the hot zone. High

temperature test specimens have been designed with a curved configuration to address this issue (Figure 3.18).

Figure 3.18: High temperature test specimen. The Al-fiber matrix is only present in the hot zone due to the curved embedding configuration, allowing the fiber exit points to be present in the center of the sample rather than at the ends.

Data taken from testing these new, coupling-limited samples matched almost exactly with the first set of samples, despite the use of the curved configuration to eliminate coupling outside of the hot zone. Data from Figure 3.19 shows mechanical coupling between the aluminum and the FBGs, and shows no difference in the strain tracking at room temperature or elevated temperatures. There was also no change in strain measurement imparted into the sensor as a result of thermal cycling, as room temperature testing before and after heating was consistent as shown in figure 3.20. The mechanical load profile during testing consisted of a steady tensile ramp up to 1000 lbs, followed by a pause, followed by a steady ramp downwards to 0 lbs

of measured force. If the acrylate coating were melted and strain transfer was accomplished by viscous effects, the measured strain by the FBG would be dependent upon the strain rate of the aluminum rather than the strain magnitude, and a drop in measured value would be expected during the pause part of the load profile. Since this drop was not observed, viscous shear transfer could be eliminated as a possibility, leaving the only other possible explanation that the coating had not undergone transition. This was found to be consistent with the behavior of UV cured acrylate in the literature.
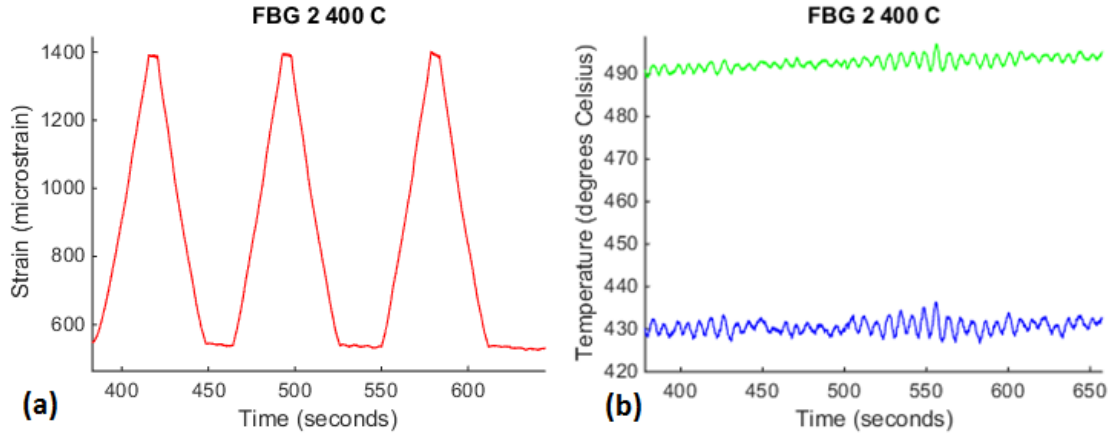
Figure 3.19: High temperature testing: (a) measured strain in FBG during cyclic 1000 lb loading and unloading at 400 degrees Celsius; (b) Measured atmospheric temperature within hot zone given 400 degrees Celsius set point at top and bottom of furnace. Temperature within the hot zone varied as a result of poor insulation on the bottom of the furnace.
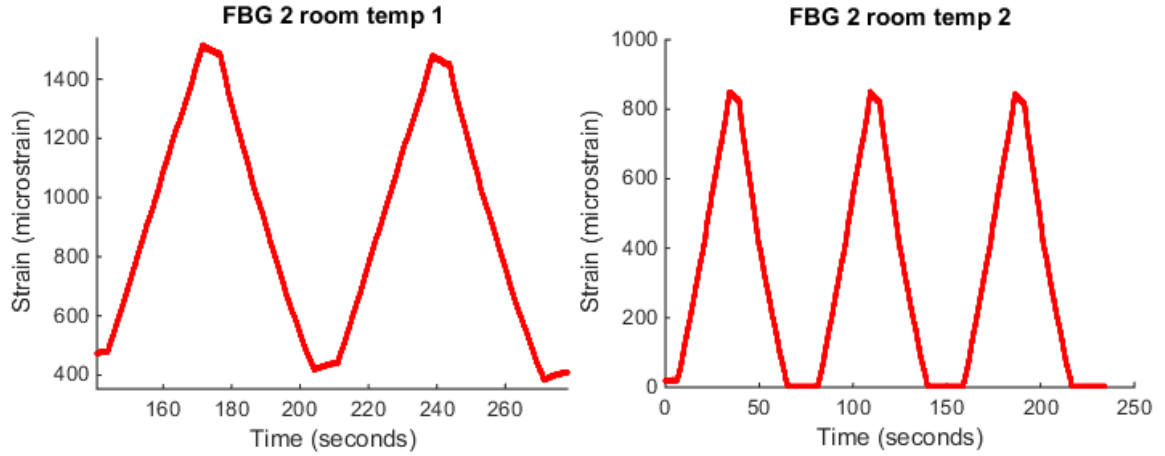
Figure 3.20: Room temperature testing following the same load profile of the 400 C tests. No change in sensor behavior was observed.

One limitation of the high temperature testing was the inability to ensure consistent temperature throughout the hot zone. Multiple thermocouples were used to ensure that the air temperature was higher than the furnace set point during tests, but thermocouples were not mounted directly to the test specimen. As such, while an exact thermocouple confirmation of internal sample temperature was impossible, the presence of internal thermal loading was confirmed by the FBG measurement in figure 3.21. Since the sample was mechanically constrained during heating, the main effect influencing reflected wavelength change was the thermo-optic effect, shown to be constant (7.33 microstrain/degree Celsius) above cryogenic temperatures in the literature. There is also little to no difference between the acrylate coating of the FBG within the hot zone vs the coating that was insulated within the grips (Figure 3.22).
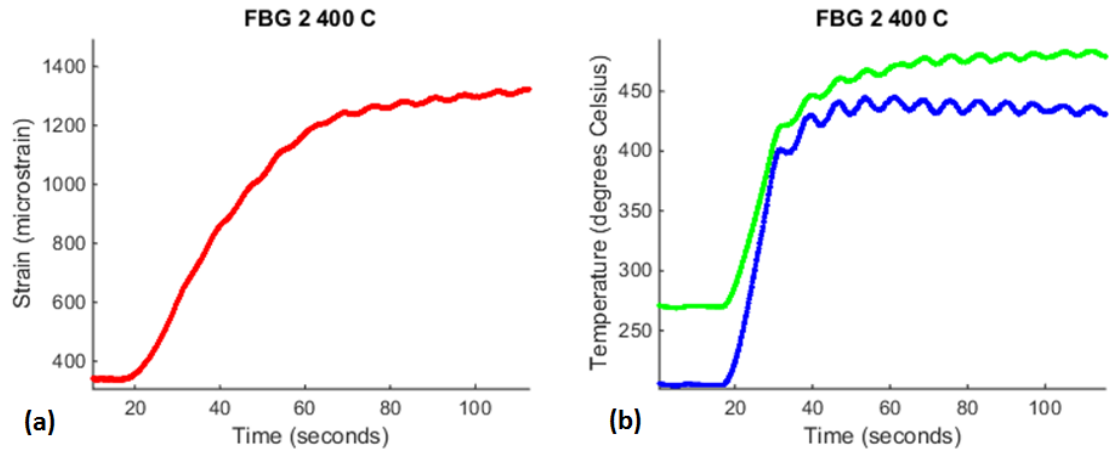
Figure 3.21: Heating profile: (a) measured strain in FBG during furnace setpoint change from 200 Celsius to 400 Celcius; (b) Measured air temperature within hot zone at top and bottom of furnace respectively.
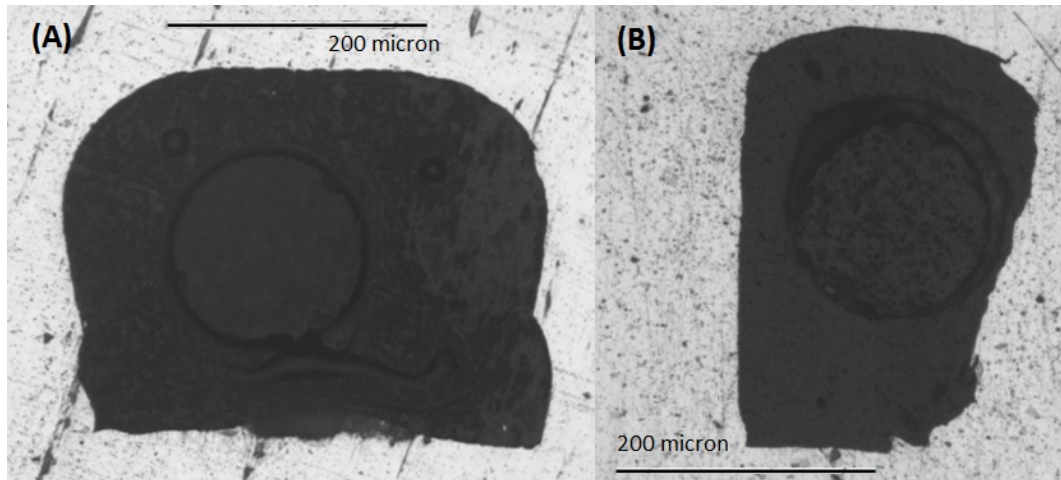
Figure 3.22: Microscopy of tensile tested samples: (A) acrylate coated sample used in high temperature testing; (B) polyamide coated sample pulled to failure.

3.4.1 FBG CTE

In order to examine the mechanical coupling between the sensor and the aluminum, a sample was thermally loaded while mechanically isolated in a lab oven. Figure 12 shows the apparent CTE of the FBG. The change in apparent CTE is due in part to the mismatch in CTE between silica glass, acrylate, and aluminum, and is also a result of thermo-optic effects leading to changes in the index of refraction of the glass [21]. At approximately 180 Celsius, the interrogator reached its maximum wavelength, and was unable to obtain higher strain measurements. Note that although the interrogator limit was reached, a clear divergence of mechanical coupling between the sensor and aluminum matrix was not observed. Future CTE testing was performed using an FBG with a nominal wavelength of 1548 nm rather than 1550 nm to improve the interrogator range.

An issue that appeared in the CTE testing is peak wavelength shifting/hopping, shown in Figure 3.23. This is a phenomenon that occurs in FBG sensors when the are subject to a non-uniform load, and the reflected wavelength profile is distorted. This peak wavelength shifting is only observed during CTE testing when the sample is either heated or cooled at too fast of a rate. This is due to the thermal inertia of the specimen resulting in a non-uniform temperature through the fiber. In addition to peak shifting, the strain profile shown in Figure 3.24 is also highly noisy and the CTE was not found to be constant.
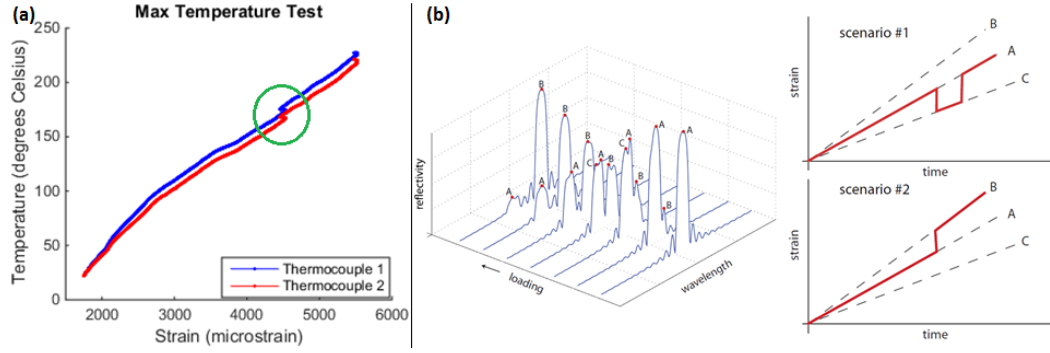
Figure 3.23: Wavelength hopping [24]: (a) CTE test data with peak shifting circled; (b) graphical representation of peak wavelength shifting: note that as the profile distorts, the measured amplitude of the spectrum changes.
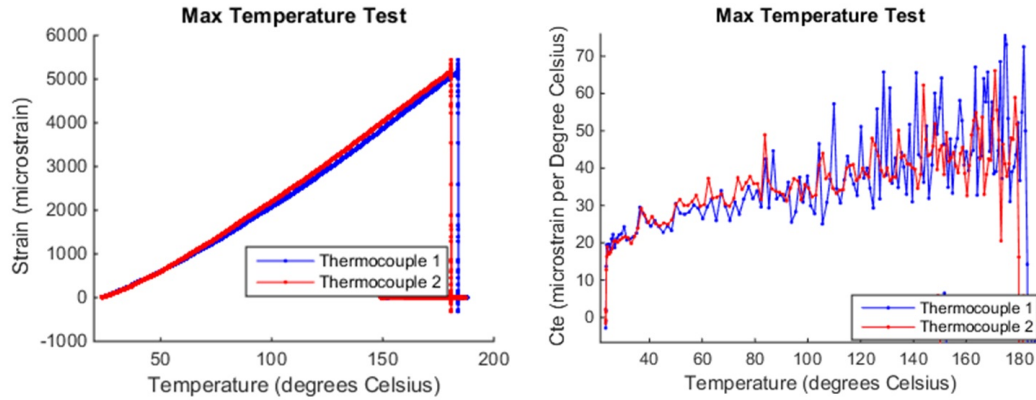
Figure 3.24: Acrylate coated sensor strain profile during mechanically unloaded heating.

In the initial oven testing, peak-wavelength shifting was observed during the thermal loading stage, but not during the thermal unloading stage. In these initial tests, the unloading took place over about twice the time period of the heating stage, which

supported the hypothesis that this shifting was a result of non-uniform loading of the sensor as a result of thermal gradients forming within the test specimen. Figures 3.25 and 3.26 show the results of a slower thermal test, in which no wavelength hopping was observed. While methods exist for extracting the total reflected profile and interpreting those results to obtain the exact strain state of the FBG sensor, the interrogator used for this study lacks that capability. A more thorough analysis of the FBG profile during fast thermal loading could be an interesting area of future work. The inability of these embedded sensors to deal with dynamic temperature situations also potentially limits the usefulness of having a mechanically isolated FBG run in parallel to obtain separate data sets. This thermally stable configuration was successful in eliminating the wavelength shifting.
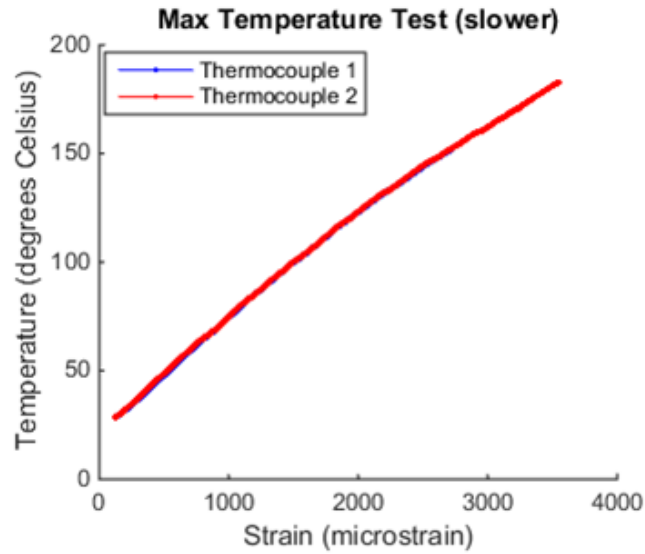
Figure 3.25: Peak wavelength shifting eliminated when the thermal profile is more stable and eliminates thermal gradients within the sample
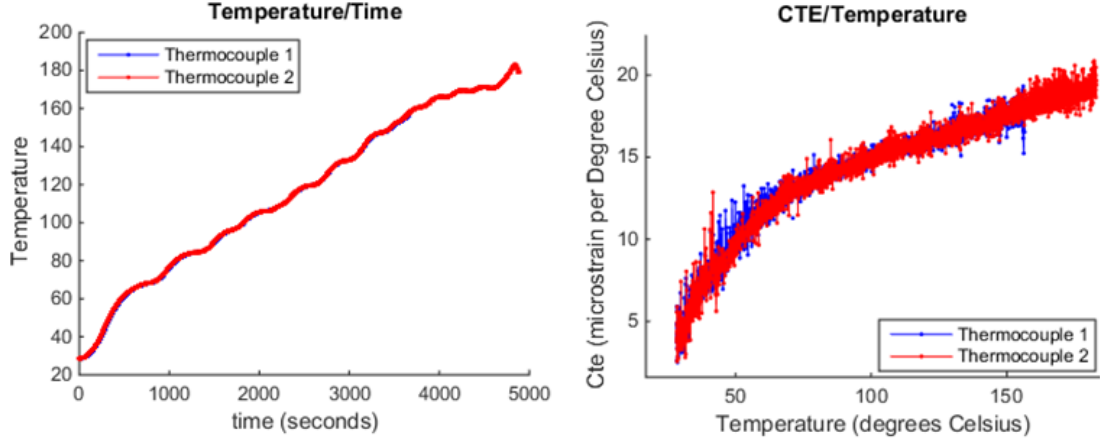
Figure 3.26: Temperature profile with respect to time and experimentally obtained CTE values for the FBG

The CTE of the embedded FBG was obtained by looking at the change in measured strain value per unit change in temperature. These values were obtained experimentally rather than empirically. The CTE of the FBG tends towards about 20 microstrain per degree Celsius, which is close to that of aluminum. This profile was consistent for both the upper and lower surface mounted K-type thermocouples.

An empirical derivation of the CTE for the FBG was made, looking at the CTE of the aluminum and the thermo-optic coefficient of the fiber. The CTE of the silica glass itself is near 0, and the stiffness of the aluminum matrix is substantial enough to overwhelm any expansion by either the glass or coating, so those values could be ignored. By examining the effects of both of these phenomenon on the change in the reflected wavelength as a result of temperature, the CTE was estimated to be approximately 25.74 microstrain per degree Celsius by the following equation:

$$\delta\gamma \div \gamma = (1 - P_e)\alpha_s\delta T + \zeta\delta T \tag{3.1}$$

Where γ is the wavelength P_e is the constant strain-optic coefficient (0.22), α_s is the CTE of aluminum (23.3), δT is the change in temperature, and ζ is the constant thermo-optic coeffcent (7.33). The predicted value does not exactly match the experimental observations, namely in that the observed CTE varies over the duration of the test. It is not clear whether this is due to the non-uniform heating of the sample, or due to some other phenomenon altering the embedded FBG CTE, such as inclusion properties changing the load subjected to the fiber. It is worth noting that the CTE of acrylate is approximately 3 times that of aluminum (75), and there may be considerable stress on the core/coating as a result of this CTE mismatch. Finally, in order to validate the temperature measurements of previous tests, the measurement from the externally mounted thermocouples were compared to that of an embedded thermocouple. While there is some variation shown in Figure 3.27, and the external sensor reaches a higher temperature than the internal sensor, they show good enough agreement to assume that the temperature of the FBG is sufficiently close to that of the external temperature.
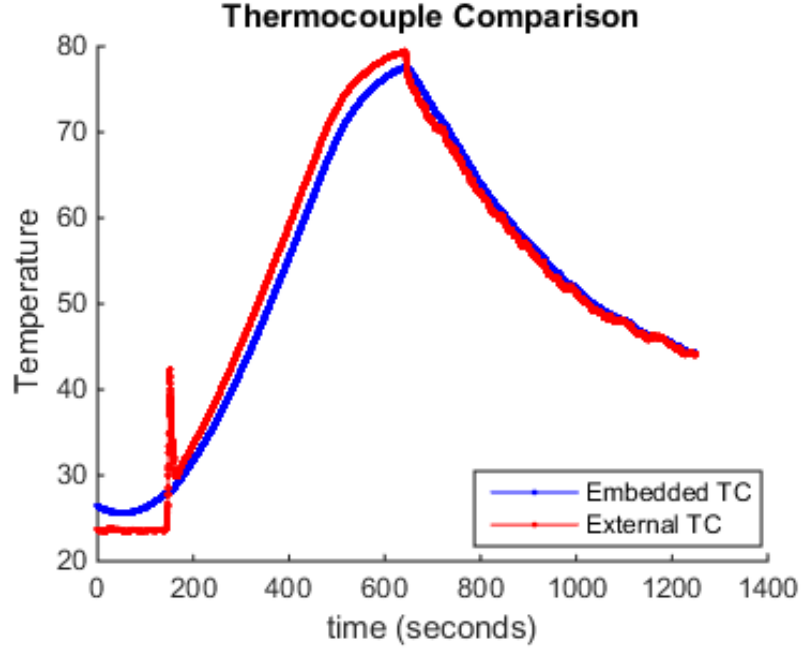
Figure 3.27: Comparison of embedded thermocouple measurement to an externally mounted thermocouple.

3.4.2 Acrylate Coating Degradation

In traditional FBG strain sensing applications, polyamide coated FBGs are chosen over acrylate coated FBGs in high temperature situations. This is a result of the difference in maximum operating temperature, which is approximately 400 degrees Celsius for polyamide and 80 degrees Celsius for acrylate. This acrylate value was initially determined by observing the glass transition behavior of acrylate. However, the acrylate used for coating FBGs is subjected to an UV cure, which alters the behavior at high temperatures. Rather than melting, UV cured acrylate degrades chemically into the atmosphere. This process has been shown to be temperature, heating rate,

and environment dependent [2]. Figure 3.28 shows fiber that was exposed to the air during high temperature testing and has degraded.
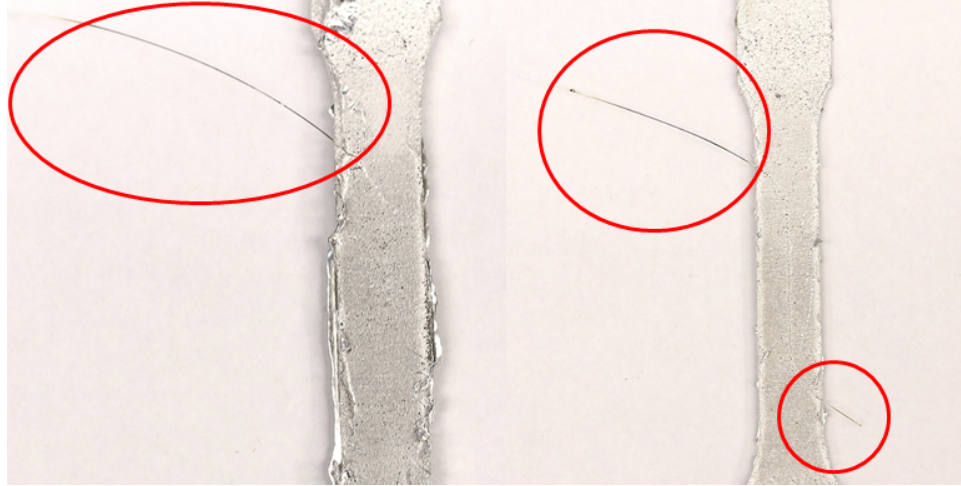
Figure 3.28: Evidence of carbonization of coating on acrylate coating exposed to air during high temperature tensile testing

Instead of glass transition followed by melting, the coating degrades or carbonizes when heat is applied. This reaction leads to a loss of mass and volume of the coating, and the rate of degradation is determined by temperature, temperature change rate, and by the environment that the coating is subjected too. Since the FBGs are embedded in aluminum and hermetically sealed within the matrix, they are not subject to any sort of gas and the degradation reaction cannot take place. This was confirmed by subjecting a test specimen to a thermal annealing at 300 degrees Celsius for over two hours, with an expected degradation amount of over 50 percent of the coating, and taking cross sections of the fiber within the aluminum and outside where it was subject to air. Figure 3.29 shows the thermal profile of the annealing, which was

confirmed by K-type thermocouples mounted externally to the sample. Some of the exposed fiber was mounted in epoxy to compare the microstructure with that of the embedded fiber. The un-encapsulated fiber shows clear evidence of carbonization, whereas the enpasulated fiber shows no changes to the dual-acrylate at all in Figure 3.30. The FBG used was through-written rather than strip/recoated, which is why two seperate acrylate areas are present in the cross section.
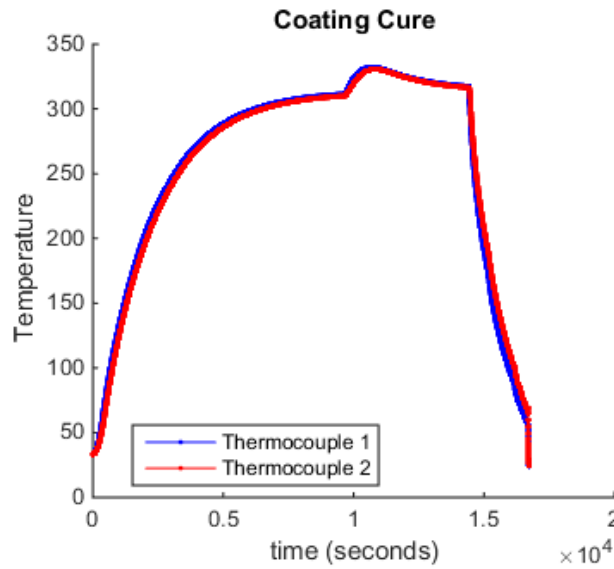
Figure 3.29: Temperature profile used to examine coating degradation of embedded FBGs with acrylate coating.
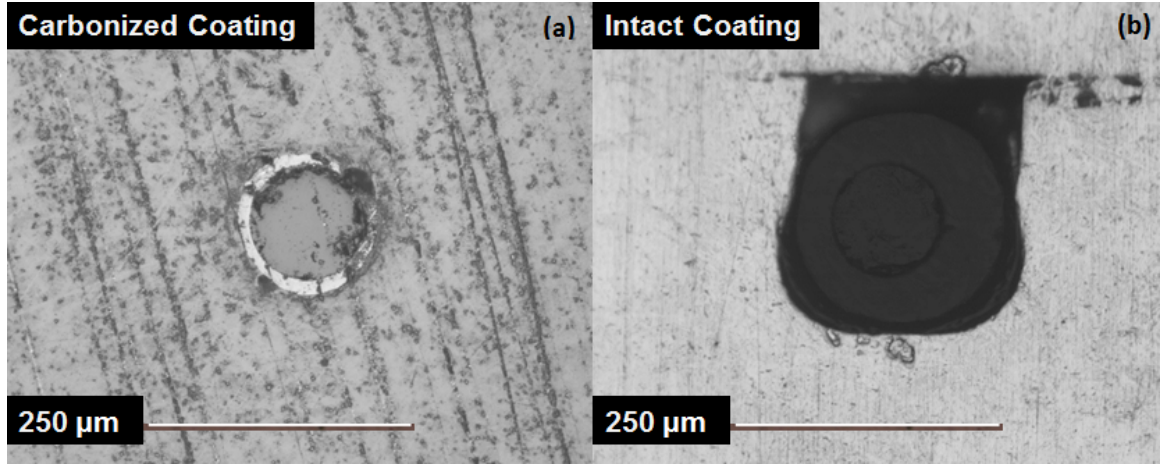
Figure 3.30: Cross sections of fiber subjected to prolonged thermal loading: (a) exposed fiber section, showing near total degradation of both layers of acrylate; (b) embedded fiber section, showing no signs of degradation of either acrylate layer.

In addition to improving the temperature range of acrylate coated FBGs, this hermetic sealing suggests that it could serve as a method for using FBGs in applications where hermetic sealing is a requirement, such as in hydrocarbon rich environments.

3.5 Manifold

In order to examine UAM embedded FBGs in a non-coupon level build, a test specimen based on a manifold style part used for flow intersection testing was developed. Due to the sample geometry, internal load confirmation must be carried out through embedded sensing. FEA analysis was performed to examine areas of stress concentration as well as search for locations suitable for FBG placement. The criteria for FBG placement were uniform loading to ensure usable measurement from the FBG, and high loading to obtain useful measurements. The FEA modeling was performed in COMSOL.

3.5.1 Modeling

The COMSOL model for the part is the following figures, with the distance unit in inches and the stress unit in Pa. The bottom of the part was fixed, and an internal pressure of 5000 psi (34.5 MPa) was introduced. The initial stress levels were dominated by the upper surface of the larger internal cylinder (Figure 3.31), which displayed a radially decaying load profile. Due to the requirement for uniform loading to obtain meaningful strain data from FBG sensors, this location was ruled out for in-situ monitoring.
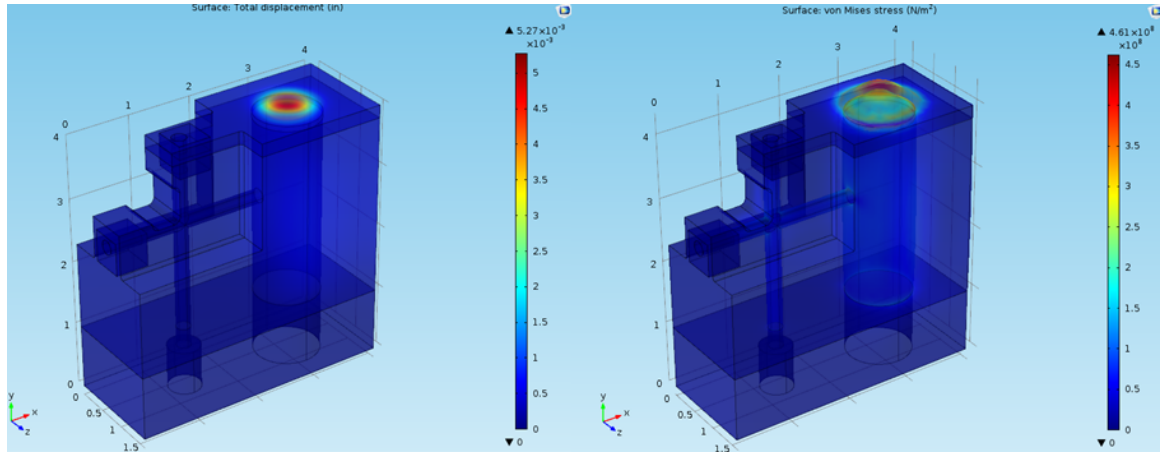
Figure 3.31: Displacement and von Mises stress of the manifold part assuming fixed bottom and internal pressure of 5000 psi. The largest load occurs at the top of the larger internal cylinder.

The top 0.25 in (6.35 mm) of the manifold were removed from the results to get a sense of the loading on the rest of the part for Figure 3.32. The displacement along the wall of the larger internal cylinder was found to be uniform and locally high, prompting it as a possible choice for an embedded FBG sensor to monitor internal

strain. A cross sectional view was used to examine the load profile of the internal cylinder wall, and confirmed uniform displacement in Figure 3.33.
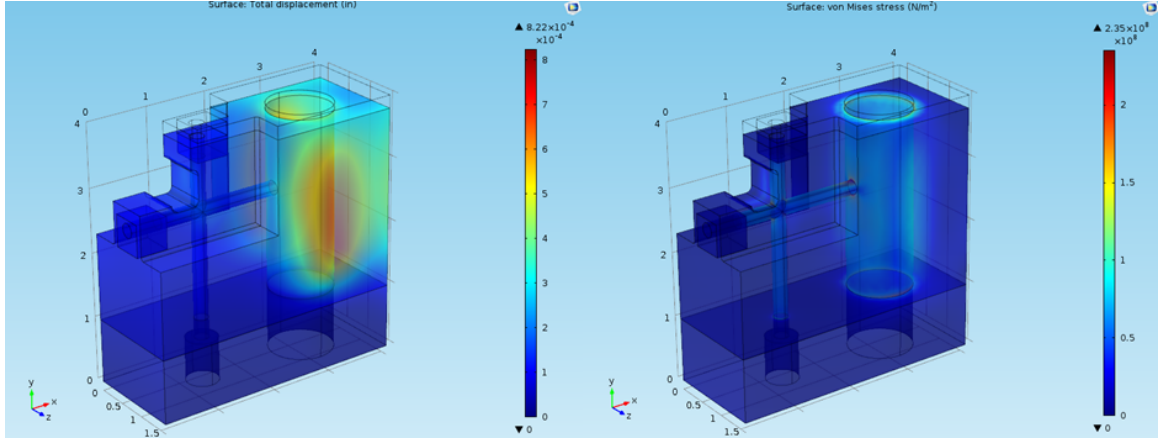
Figure 3.32: Displacement and von Mises stress contours neglecting the top cylindrical surface. The largest displacement occurs along the wall of the internal cylinder, and stress concentrations are visible throughout the internal channels of the part.
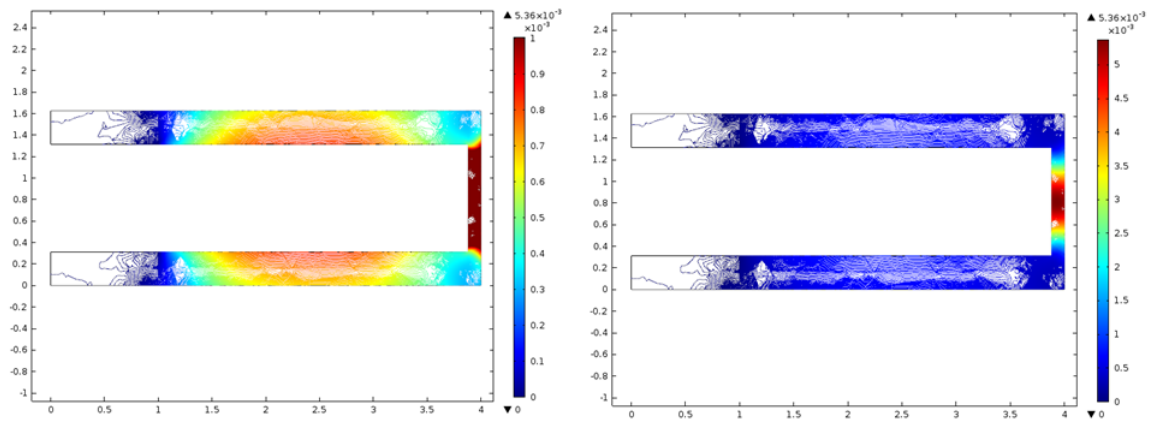
Figure 3.33: Scaled and unscaled displacements looking at a cross section of the larger internal cylinder.

The final locations of interest were the internal channels near the point of flow intersection. In order to obtain a sense of the loading at these internal channels, both the x and y components of stress were modeled in a cross sectional cut of the middle of the part as shown in Figure 3.34. While uniform stress concentrations were seen along the walls of these channels, the loading was less than that of the larger cylinder wall and dispersed through a lesser depth. As such, an FBG sensor placed to measure loads would need to be encapsulated with very limited support. As a result of the specimen geometry, a much larger percentage of the part would have to be made through UAM as well, which could impact the structural integrity of the part at large internal pressures.
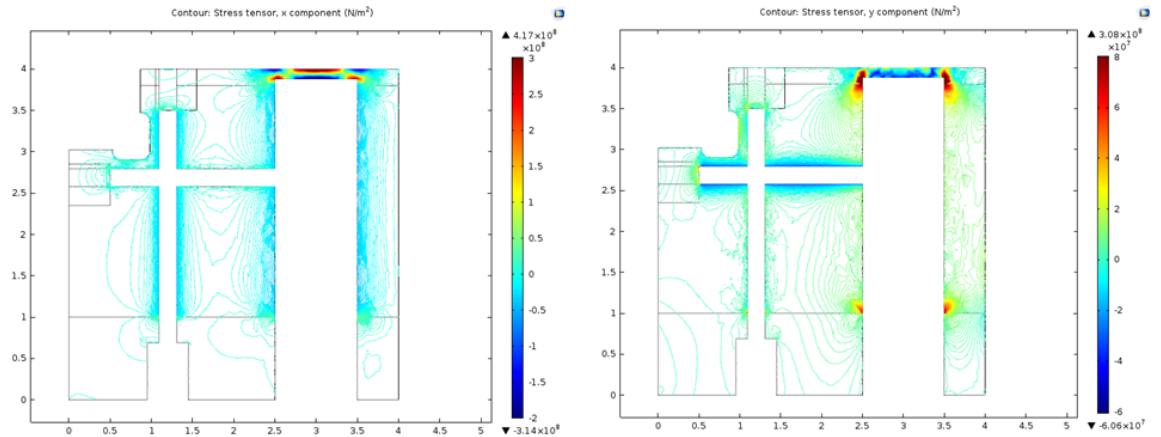
Figure 3.34: X and Y components of stress along a cross-sectional view of the manifold. The flow intersection channels show some loading, but it is concentrated along a very small depth relative to the part thickness.

Following this analysis, the sensor location was chosen to be along the larger internal cylinder wall. In order to validate the ability of an FBG to obtain uniform

strain measurements, the load profile of the cross-section of the internal cylinder with an integrated fiber was examined (Figure 3.35). The model showed uniform loading on the fiber along the area of interest, which is to be expected given a loading area larger than the shear lag threshold.
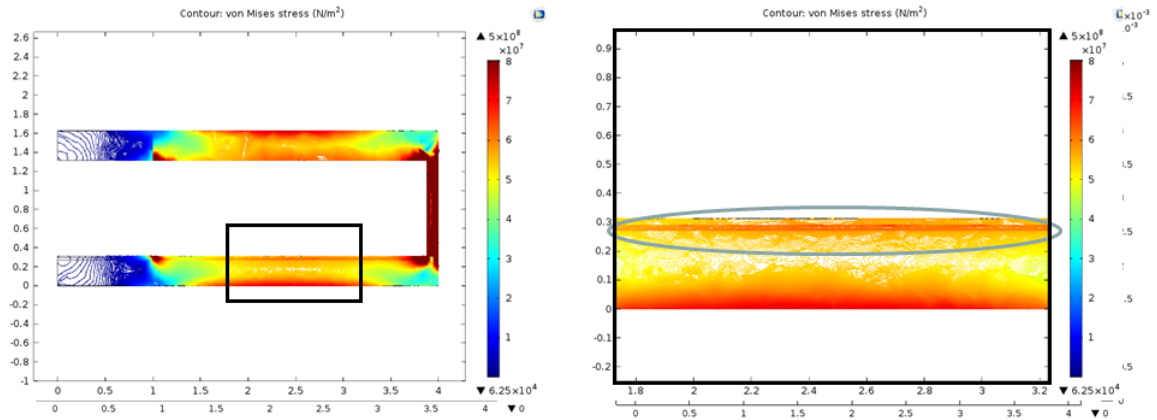
Figure 3.35: FEA Model of the manifold with an optical fiber included. The model shows strain transfer between the part and fiber, which is consistent with shear lag expectations.

Part of the future work on this project includes the fabrication and testing of these manifold test specimens via UAM.

Chapter 4: CONCLUDING REMARKS

4.1   Summary

FBG sensors were embedded into aluminum test specimens through the UAM process. UAM was chosen for its ability to join metals, low process temperature, and integrated subtractive operations, which allow for the fabrication of smart metallic structures. The embedded FBG sensors were characterized by comparison to foil strain gages and determination of performance limits. Cantilever bending testing showed that the strain profiles between foil gages and FBGs matched, and tensile testing showed that the measured strain values were shared as well. Birefringence effects showed the need for an embedding channel prior to encapsulation in order to minimize cross-sectional deformation of the fiber, and no adverse effects were observed in the embedment of fiber into curved channels. High temperature testing showed no evidence of inscription reversal, and cross-sections of thermally loaded samples indicated that embedded FBG sensors do not carbonize at expected temperatures due to the lack of a gas environment.

4.2 Future Work

This study serves as a benchmark in the characterization of embedded sensors used in ultrasonic additive manufacturing applications. While there is value in proving that FBGs can be incorporated into matrix material as a concept, the matrix behavior of bulk material is sufficiently different from that of 3D printed material that it is critical to show that the signal obtained from the sensor actually corresponds to the states of the material. Given the difficulties inherent to incorporating FBG sensors into metallic components through traditional manufacturing methods, it was therefore necessary to characterize the FBG values through the use of a different type of sensor. One way to potentially improve the comparative data used for this characterization would be to use a sensor mounted in the same cross-sectional position as the FBG, rather than the sensor. Other types of strain measurement could also be applied, such as Differential Image Correlation. Embedding an FBG without the external coating could also be of some value, although it is incredibly likely that substantial issues will exist with birefringence if the glass is in direct contact with the aluminum. Lastly, by using more advanced methods of FBG interrogation, which can look at the overall spectrum rather than just the highest intensity reflected wavelength, more data can be obtained from the sensor during dynamic loading.

The long term behaviour of embedded FBG sensors is also not well documented. Using the sensors for either fatigue or durability testing would be extremely useful in terms of in-situ sensing, and documenting their performance compared to existing methods of load detection could be valuable. It is also not clear what the impact on long term performance of a metallic structure is as a result of having discontinuities in the matrix due to an embedded FBG. In situ sensing would provide little benefit if

the lifetime of the structure is considerably shortened as a result, and any application using embedded sensors should look at the long term effects on the structure.

In addition to improving upon the research corresponding to FBGs, many of the techniques and tests performed can be directly applied to alternative types of sensors. The hermetic sealing aspect of UAM also presents interesting possibilities for sensors or materials that can be improved through embedment. Either by delaying transformation/degradation of certain materials at higher temperatures, or allowing embedded circuits that require a sealed environment to function, UAM has now been shown to offer some otherwise unexpected opportunities for part design.

Finally, the ultimate goal of this research is to encourage novel techniques of SHM. The fabrication of smart structures with integrated sensor networks is only recently possible with the advent of 3D printing, and creates a new design space with opportunities for drastically improving the lifetime, reliability, and safety of structures. Non-destructive evaluation has become a several billion dollar industry, and the logical progression is to create vehicles and systems capable of analyzing themselves. As advances are made in sensor performance and in our ability to build sensors into components, smart vehicles will become the new standard.

Bibliography

[1] D. Karalekas A. Kantaros. Fiber bragg grating based investigation of residual strains in abs parts fabricated by fused deposition modleing process. *Materials and Design*, 50(44), 2013.

[2] D.A. Simoff A.A. Stolov and J. Li. Thermal stability of specialty optical fibers. *Journal of Lightwave Technology*, 26.20, 2008.

[3] G.P. Agrawal. *Fiber-optic communication systems*, volume 222. John Wiley and Sons, 2012.

[4] E. Bayo and L. Leka. A close look at the embedment of optical fibers into composite structures. *Journal of Composites, Technology and Research*, 11.3, 1989.

[5] D. Li K. Zhou L. Zhang-R. Soar C. Mou, P. Saffari and I. Bennion. Smart structure sensors based on embedded fibre Bragg grating arrays in aluminium alloy matrix by ultrasonic consolidation. *Measurement Science and Technology*, 20.3, 2009.

[6] K. Chawla. *Composite materials: science and engineering*. Springer Science and Business Media, 2012.

[7] X. Cheng and X. Li. Micro thin film sensor embedded in metal structures for in-situ process monitoring during ultrasonic welding. In *ASME 2005 International Mechanical Engineering Congress and Exposition*, pages 1117–1121. American Society of Mechanical Engineers, 2005.

[8] W.N. MacPherson D.P. Hand D. Havermann, J. Matthew and R.R.J. Maier. Measuring residual stresses in metallic components manufactured with fibre bragg gratings embedded by selective laser melting. In *International Conference on Optical Fibre Sensors (OFS24)*, pages 96340T–96340T. International Society for Optics and Photonics, 2015.

[9] K. Graff. *ASM Handbooks: Volume 6A, Welding Fundamentals and Processes*. American Society for Materials International, 2011.

[10] D. Huston. *Structural sensing, health monitoring, and performance evaluation.* CRC Press, 2010.

[11] H. Choi W. Cai J.A. Abell J.Zhao, H. Li and X. Li. Insertable thin film thermocouples for in situ transient temperature monitoring in ultrasonic metal welding of battery tabs. *Journal of Manufacturing Processes*, 15(1):136–140, 2013.

[12] T. Hosaka K. Okamoto and T. Edahiro. Stress analysis of optical fibers by a finite element method. *IEEE Journal of Quantum Electronics*, 17.10, 1981.

[13] Raman Kashyap. *Fiber Bragg Gratings.* Academic press, 1999.

[14] C.Y. Kong and R.Soar. Method for embedding optical fibers in an aluminum matrix by ultrasonic consolidation. *Applied Optics*, 44(30), 2005.

[15] K. Kuang and W. Cantwell. Use of conventional optical fibers and fiber Bragg gratings for damage detection in advanced composite structures: a review. *Applied Mechanics Reviews*, 56(5), 2003.

[16] G.D. Lloyd. Resonant cavity fibre bragg grating sensor interrogation. 2004.

[17] N. Gowripalan P. Childs, A.C.L. Wong and G.D. Peng. Measurement of the coefficient of thermal expansion of ultra-high strength cementitious composites using fibre optic sensors. *Cement and Concrete Research*, 37.5, 2007.

[18] A.J. Hehr P.J. Wolcott and M.J. Dapino. Optimized Welding Parameters of Al 6061 Ultrasonic Additive Manufactured Structures. *Journal of Materials Research*, 29(18), 2014.

[19] S. Demokan P.K. Ko and H. Tam. Distributed temperature sensing with erbium-doped fiber amplifiers. *Journal of Lightwave Technology*, 14.10, 1996.

[20] J.S. Sirkis C.S. Baldwin J.R. Troll-R. Grande C.S. Davis R.C. Foedinger, D.L. Rea and T.L. Vandiver. Embedded fiber optic sensor arrays for structural health monitoring of filament wound composite pressure vessels. In *1999 Symposium on Smart Structures and Materials*, pages 289–301. International Society for Optics and Photonics, 1999.

[21] M.B. Reid. Temperature dependence of fiber optic bragg gratings at low temperatures. *Optical Engineering*, 37(1):237–240, 1998.

[22] S.S.J. Roberts and R. Davidson. Mechanical properties of composite materials containing embedded fiber-optic sensors. In *OE Fiber-DL tentative*, pages 326–341. International Society for Optics and Photonics, 1991.

[23] J.S. Barton M. Carne M. Swan-J.N. Sharma S.K. Futter D.A. Knox B.J.S. Jones R.R.J. Maier, W.N. MacPherson and S. McCulloch. Embedded Fiber Optic Sensors Within Additive Layer Manufactured Components. *IEEE Sensors Journal*, 13(3), 2013.

[24] M. Zikry T. Vella S. Chadderdon-R. Selfridge S. Webb, K. Peters and S. Schultz. Wavelength hopping due to spectral distortion in dynamic fiber bragg grating sensor measurements. *Measurement Science and Technology*, 22.6(065301), 2011.

[25] S.J. Hu W.W. Cai S.S. Lee, T.H. Kim and J.A. Abell. Analysis of weld formation in multilayer ultrasonic metal welding using high-speed images. *Journal of Manufacturing Science and Engineering*, 137(3):031016, 2015.

[26] T.H. Kim S.J. Hu E. Kannatey-Asibu W.W. Cai J.P. Spicer S.S. Lee, C. Shao and J.A. Abell. Characterization of ultrasonic metal welding by correlating on-line sensor signals with weld attributes. *Journal of Manufacturing Science and Engineering*, 136(5):051019, 2014.

[27] ASTM Standard. E8/e8m, 2009. standard test methods for tension testing of metallic materials. astm international, west conshohocken pa; 2009. doi: 10.1520. Technical report, E0008-E0008M-09, www. astm. org.

[28] K.V. Wong and A. Hernandez. A review of additive manufacturing. *ISRN Mechanical Engineering*, 2012.

[29] D.K. Liang X.W. Pan and D.Li. Optical fiber sensor layer embedded in smart composite material and structure. *Smart materials and structures*, 15(5):1231, 2006.

[30] G. Zhou and L.M. Sim. Damage detection and assessment in fibre-reinforced composite structures with embedded fibre optic sensors-review. *Smart Materials and Structures*, 11(6):925, 2002.

Appendix A: EXTENDED PROCEDURES

This section serves to explain some of the subtleties involved with performing FBG sensing as shown in this document. Some brief instruction on working the interrogator, various issues with signaling, common setup issues/errors, and sanity checks to ensure quality, expedited testing are all included.

A.0.1 Interrogator

Some quality documentation on working the interrogator exists, and rather than retype it here I invite the reader to contact either myself or Insensys to obtain a copy. That being said, some of the finer details are worth mentioning. The interrogator used is an insensys model OEM 1030. This interrogator works off of time division multiplexing /citeLloyd and was designed for wind turbine strain monitoring, and as such exports all data into a digital signal. It runs off of the computer's internal clock for a time signal, which means that either some post-processing or a digital to analog converter circuit is required in order to obtain time independent data. There is also a limit on the interrogator in terms of wavelength, as the interrogator can only measure from 1540 to 1550 nm. For high load or high temperature testing, using 1542 nm nominal wavelength FBGs is recommended. Note that if you exceed the

wavelength limit, the interrogator lights will turn red and will remain that way until the wavelength reaches a measurable level.

To operate the interrogator, first insert the end of the FBG into one of the channels. There should be two clicks to ensure that the FBG is fully inserted, and the plug-release will pop up. After the FBG is fully inserted, select the active channel as whichever channel you inserted the FBG into, and then run 'scan for sensors'. After a short delay, the FBG should appear with the nominal wavelength that you expect. The interrogator can either take data to the screen (which will save to a location in temp/virtualstore), or can be set to 'stream data'. Setting the interrogator to stream will allow you to disconnect the main cord and replace it with the digital to analog converter if you are using one. The first check you should do if you're data isn't appearing in whichever data acquisition program you are running to take data, assuming you are using a converter, is to make certain that you have actually plugged the digital to analog converter into the interrogator.

A.0.2 Digital to Analog Converter

This piece of hardware allows you to obtain analog data from the interrogator, a requirement for synching up the time signals of the various sensors you will be using. The digital to analog converter will output a voltage based on the change of the measured wavelength from when it was first powered. That means that the 0 strain wavelength is whatever the wavelength happens to be when the circuit is powered on, NOT the nominal wavelength of the FBG. If you are powering on the converter after loading a sample into test grips, for example, make certain to note the true strain on the FBG and manually adjust your data accordingly. The converter is limited to

an output of 3.3 volts, and can be operated in one of two modes: Full tensile, where the nominal value is taken to be 0 volts, or tensile/compressive, where the nominal value is taken to be 1.65 Volts. The converter can take on different scale factors as well, and should be verified with comparative foil gage strain measurement whenever possible. The equations for scaling the converter data are:

$$\delta\gamma = 4096 * 3.3 * V \tag{A.1}$$

$$\epsilon = 0.845 * \delta\gamma \tag{A.2}$$

Where $\delta\gamma$ is the wavelength shift in nanometers, V is the voltage in volts, and ϵ is the strain in microstrain. As a final note, if you wish to do high range testing at a small measurement scale, the nominal value of strain can be reset by depowering and repowering the converter.

A.0.3 Polarization Controller

Operation of the manual polarization controller is fairly straightforward. Make sure not to adjust the knobs on the paddles, as doing so will change the induced loading on the fiber. To change the polarization of the light, alter the position of the paddles using a waggling motion. This induces arbitrary polarizations to the data, and after a wide range of positions the overall change in strain measurement as a result of birefringence should be established. Note that it will be necessary to rerun the 'scan for sensors' program in the interrogator when moving an FBG from the interrogator to the polarization controller, as the relative position of the sensor

from the interrogator (overall length of optical fiber between the interrogator and the sensor) will have changed.

A.0.4   Specimen Fabrication

Building UAM samples with embedded FBGs is somewhat of an art, as a result of their extreme fragility compared to the mechanical loads associated with high power UAM. Firstly, ensure that the sensor is functioning prior to embedment, and note the exact nominal wavelength, as it is subject to change from during welding as previously shown. After welding at least 0.010 inches of tape to ensure a consistent UAM matrix is observed by the fiber, a channel should be cut using a 0.010 inch diameter mill bit. To maximize tool life, this channel should be cut at 8000 rpm, 0.5 inches per minute feed rate, and at a depth no greater than 0.005 inches. This means that two separate cutting passes should be performed for a single channel. After this channel is built, insert the fiber with the sensor at the desired location. This is accomplished by gently rolling the fiber into the channel. When embedding the sensor in a curved configuration, such as the high temperature specimens shown in this thesis, I suggest placing the fiber in one of the curves, and then pushing the rest of the fiber along while keeping one of your fingers over the initial fiber. The fiber will have a tendency towards straightening out if you don't do this, but once the fiber is placed snugly into both curves it will hold itself in nicely. Verify channel height/sensor placement by running your nail over the fiber along the sample. After the fiber is placed in the channel, use tape to secure the sensor and act as a strain relief.
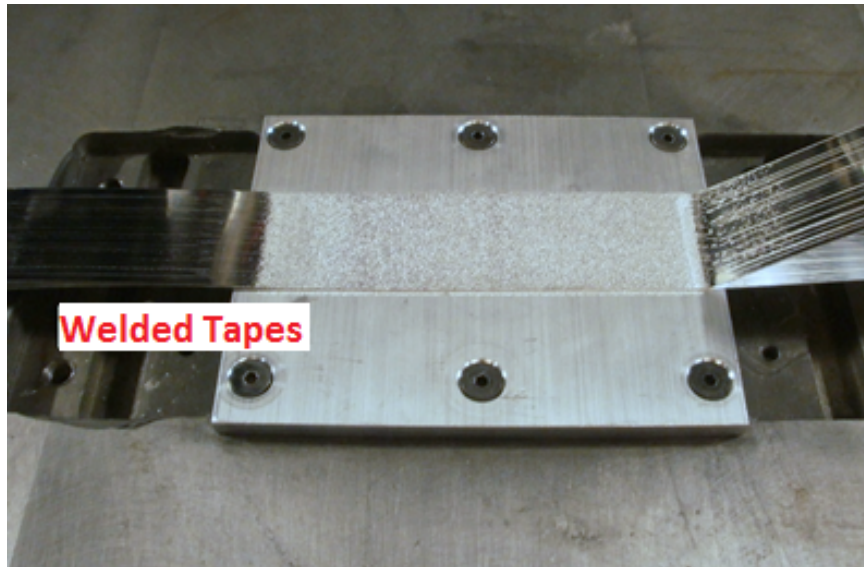
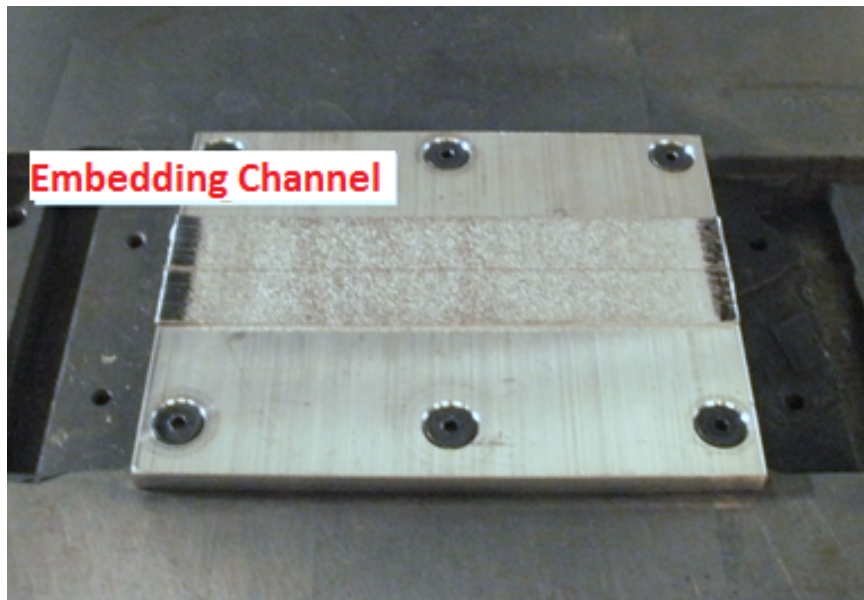Figure A.1: Baseplate for building FBG samples.

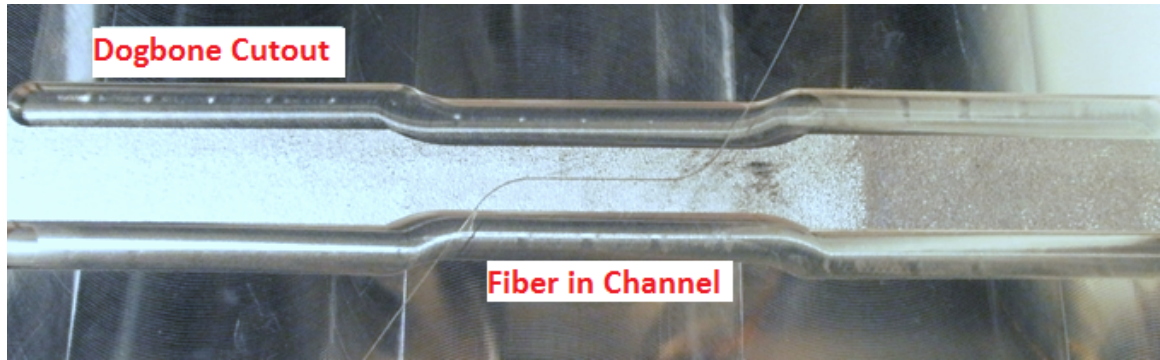Figure A.2: Channel for fiber placement.

Figure A.3: Specimen traced prior to FBG placement.

I also recommend having the outline of your specimen cut out prior to welding the encapsulating layer of tape, as it is prohibitively difficult to cut exactly around the fiber after it is built into the sample. Also, using a fixture to machine out the back of the specimen with CNC rather than hand milling is both faster and has a higher success rate. Hand milling out the sample can lead to it dropping, and manual cutting operations increase the chance of breaking the fiber at its exit location. When doing the milling operations, ensure that at least 0.004 inches of material is left above the baseplate or you risk tearing the material during welding. Tearing the material in such a way will break the vacuum seal and ruin the ability of that plate to take welds.
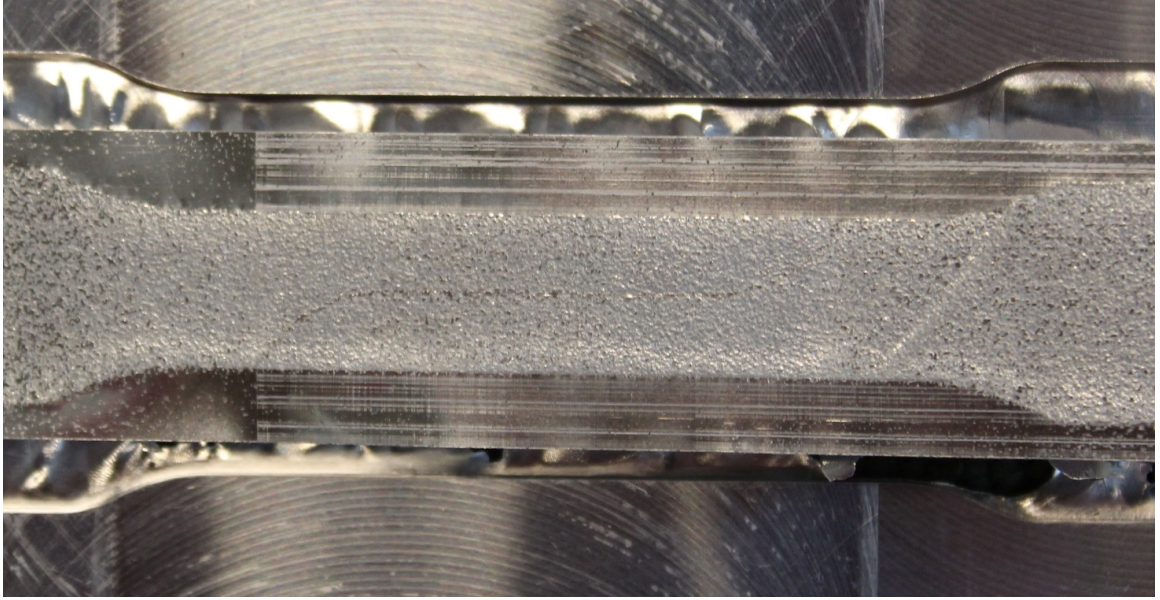
Figure A.4: Tearing caused by welding over a sample that was traced too deeply.

Please note that the flexibility of FBGs makes them functionally easier to embed than some other sensors. K-type thermocouples of the thicker type are exceptionally difficult to keep in place during welding as they have a tendency to stick out of their channels.

Figure A.5: Channels for placement of both FBG and thermocouple.

A.0.5 Data Artifacts

There are some issues with exporting the data to matlab that occur when using the higher resolution settings of the digital to analog converter. When the circuit output reaches 3.3 volts, it must be re-zeroed by unplugging the usb port of the converter and plugging it back in. This will reset the value to zero, and thus the final strain value prior to the reset should be added at this point to create the continuous strain profile.

Finally, the circuit will occassionally short itself, which will result in zero strain measurements output. Because the power is not reset, when the circuit corrects itself when it starts measuring again and the strain values it outputs will be correct. Do not re-zero the converter when this occurs, and simply use Matlab's built in figure editing

tools to delete the incorrect data artifacts. An example of this is shown in Figure
A.6. In order to ensure that the data profile measured is consistent and continuous,
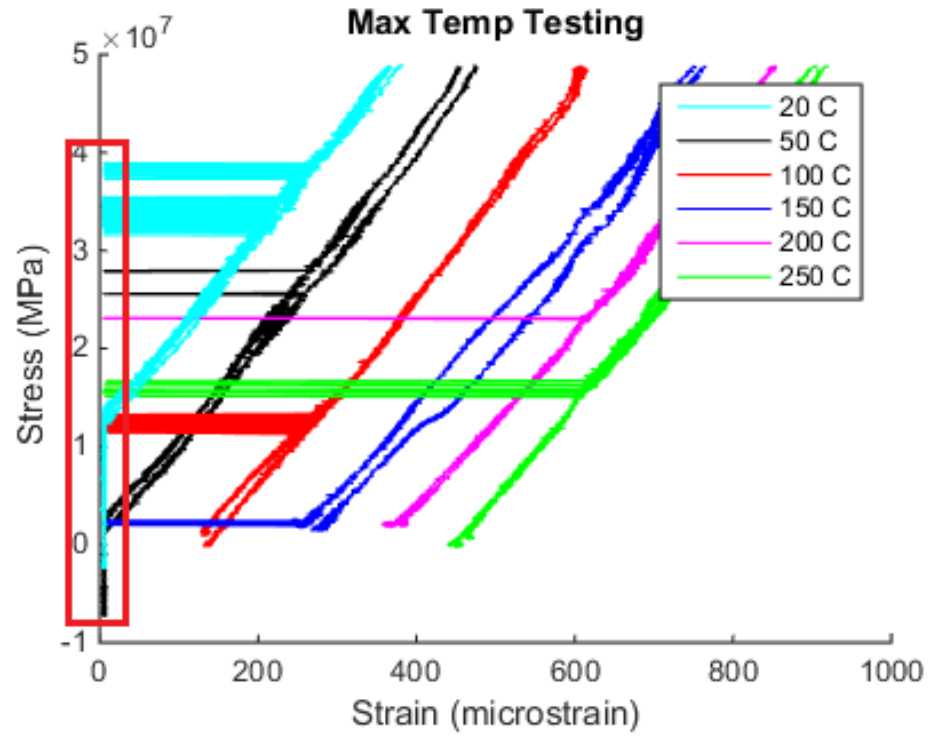it is the author's suggestion that each test be run a few times in a row when possible.

Figure A.6: Data with occasional loss of signal. The boxed area represents false zero
strain measurements.